Multigenetic Origin of the X-discontinuity Below Continents: Insights from African Receiver Functions

Stephen Pugh[1], Alistair Boyce[1], Ian David Bastow[2], Cynthia Ebinger[3], and Sanne Cottaar[1]

[1]University of Cambridge
[2]Imperial College London
[3]Tulane University

December 7, 2022

Abstract

Constraints on chemical heterogeneities in the upper mantle may be derived from studying the seismically observable impedance contrasts that they produce. Away from subduction zones, several causal mechanisms are possible to explain the intermittently observed X-discontinuity (X) at 230-350km depth: the coesite-stishovite phase transition, the enstatite to clinoenstatite phase transition and/or carbonated silicate melting, all requiring a local enrichment of basalt. Africa hosts a broad range of terranes, from Precambrian cores to Cenozoic hotspots with or without lowermost mantle origins. With the absence of subduction below the margins of the African plate for >0.5Ga, Africa presents an ideal study locale to explore the origins of the X.

Traditional receiver function (RF) approaches used to map seismic discontinuities, like common conversion-point stacking, ignore slowness information crucial for discriminating converted upper mantle phases from surface multiples. By manually assessing depth and slowness stacks for 1° radius overlapping bins, normalized vote mapping of RF stacks is used to robustly assess the spatial distribution of converted upper mantle phases. The X is mapped beneath Africa at 233-340km depth, revealing patches of heterogeneity proximal to mantle upwellings in Afar, Canaries, Cape Verde, East Africa, Hoggar, and Réunion with further observations beneath Cameroon, Madagascar, and Morocco. There is a lack of an X beneath southern Africa, and strikingly, the magmatic eastern rift branch of the southern East African Rift. With no relationships existing between depth and amplitudes of observed X and estimated mantle temperatures, multiple causal mechanisms are required across a range of continental geodynamic settings.

Multigenetic Origin of the X-discontinuity Below Continents: Insights from African Receiver Functions

Stephen Pugh[1], Alistair Boyce[1,2], Ian D. Bastow[3], C. J. Ebinger[4], Sanne Cottaar[1]

[1]Bullard Laboratories, Department of Earth Sciences, University of Cambridge, UK
[2]Université Lyon 1, ENS de Lyon, CNRS, UMR 5276 LGL-TPE, F-69622, Villeurbanne, France
[3]Department of Earth Science and Engineering, Imperial College, London, UK
[4]Department of Earth and Environmental Sciences, Tulane University, New Orleans, LA, USA

Key Points:

- P-to-S converted receiver functions reveal the X-discontinuity beneath the East African Rift System, Morocco, Cameroon, Hoggar and several ocean islands
- Observations are collocated with recent surface magmatism suggesting widely distributed chemical heterogeneity below Africa
- No relationships exist between depth and amplitudes of observed X and estimated temperatures, suggesting multiple causal mechanisms

Corresponding author: Stephen Pugh, `sdp43@cam.ac.uk`

Abstract

Constraints on chemical heterogeneities in the upper mantle may be derived from studying the seismically observable impedance contrasts that they produce. Away from subduction zones, several causal mechanisms are possible to explain the intermittently observed X-discontinuity (X) at 230–350 km depth: the coesite-stishovite phase transition, the orthorhombic enstatite to high-pressure clinoenstatite phase transition and/or carbonated silicate melting, all of which require a local enrichment of basalt. Africa is host to a broad range of terranes, from Precambrian cores to Cenozoic hotspots with or without lowermost mantle origins. With the absence of subduction below the margins of the African plate for >0.5 Ga, Africa presents an ideal study locale to explore the origins of the X.

Traditional approaches used to map the spatial distribution of horizontal discontinuities observed by receiver functions (RFs), like common conversion-point stacking, ignore the slowness information crucial for discriminating converted upper mantle phases from surface bouncing multiples. By manually assessing depth and slowness stacks for overlapping bins of 1° radius, a normalized vote mapping approach of RF stacks is used to robustly assess the spatial distribution of converted upper mantle phases. The X is mapped beneath Africa between 233 and 340 km depth, revealing patches of heterogeneity proximal to mantle upwellings in Afar, Canaries, Cape Verde, East Africa, Hoggar, and Réunion with further observations beneath Cameroon, Madagascar, and Morocco. There is a lack of an X beneath the whole of southern Africa, and strikingly, the magmatic eastern rift branch of the southern East African Rift. With no relationships existing between depth and amplitudes of observed X and estimated mantle temperatures, multiple causal mechanisms are required across a range of continental geodynamic settings.

Plain Language Summary

Local variations in the mineral chemistry of the upper mantle results in sharp changes in velocity and density. Seismic waves that convert from compressional-to-shear wave propagation (P-to-S) in the upper mantle are sensitive to these jumps in velocity and density, revealing variations in mineral chemistry. One such jump in velocity and density, the X-discontinuity, has several proposed explanations and detecting its presence across a range of mantle conditions allows us to test these possible hypotheses.

We search for observations of the X-discontinuity, where P-to-S conversion occurs between 230–350 km depth, beneath the continent of Africa. Our observations are found beneath many regions of surface magmatism across Africa, suggesting that the X-discontinuity has multiple origins.

1 Introduction

1.1 Overview

Mineral phase transitions cause abrupt jumps in local velocity and density structure of the mantle. The seismically observable impedance contrasts resulting from these transitions are termed seismic discontinuities. Due to estimated pressure-temperature dependence of discontinuity depth, the uplift or depression of some global seismic discontinuities can be studied as a thermometer for local mantle structure (e.g., Helffrich, 2000, 2002). On the other hand, non-global, localized seismic discontinuities can map the local enrichment of chemical heterogeneity, such that the impedance contrast of the seismic discontinuity renders it seismically observable. One such non-global discontinuity at 230–350 km depth is the X-discontinuity (X; e.g., Revenaugh & Jordan, 1991; Deuss & Woodhouse, 2004; Schmerr, 2015) that may be used as a tracer for upper mantle chemical heterogeneity, the distribution of which may shed important insights into mantle dynamics and the extent of chemical equilibration.

Prior observations of the X-discontinuity have been concentrated in the oceans (Deuss & Woodhouse, 2002; Schmerr et al., 2013; Schmerr, 2015; Pugh et al., 2021). While observations of the X at subduction zones are thought to track hydration reactions (Revenaugh & Jordan, 1991) and eclogite (Schmerr et al., 2013) in downgoing plates, importantly, observations of the X above mantle plumes may inform us about both the distribution of chemical heterogeneity in the lower mantle and its subsequent transportation to the upper mantle (e.g. C. D. Williams et al., 2019; Pugh et al., 2021). In regions of elevated mantle temperatures, several causal mechanisms have been proposed to explain observations of the X including the coesite-stishovite (Co-St) phase transition (Q. Williams & Revenaugh, 2005), orthorhombic enstatite to high-pressure clinoenstatite pyroxene (OEN-HCEN) phase transition (Woodland, 1998) and the deep formation of partial melts (e.g., Dasgupta et al., 2013). For further discussion of causes of the X-discontinuity away from elevated temperatures see Schmerr (2015), Kemp et al. (2019) and Pugh et al. (2021).

In contrast to the oceans, studies of the X-discontinuity in continental hotspot settings have received comparatively little attention (e.g., Rein et al., 2020), due to sampling deficiencies in reflected phase studies (e.g., Schmerr, 2015) and the distribution of overlying stations required for converted phase studies. Africa presents the perfect study locale to search for the X because it is host to widely distributed Cenozoic magmatism (e.g., Ebinger & Sleep, 1998; Furman et al., 2006; Pik et al., 2006; de Gouveia et al., 2018), with debated thermochemical nature, origin/scale depth (e.g., Simmons et al., 2007; Civiero et al., 2015; Boyce et al., 2021) and geodynamic causal mechanism (Fairhead & Binks, 1991; Ebinger & Sleep, 1998; King & Anderson, 1998; King & Ritsema, 2000; Gallacher & Bastow, 2012; Milelli et al., 2012). For example, Boyce et al. (2021) propose that a hot, chemically distinct upwelling beneath the southern East African Rift System (EARS; Figure 1b) is sourced from the African LLVP, while magmatism in Ethiopia may lie above an additional purely thermal upwelling whose depth extent is uncertain. Elsewhere, smaller volume magmatism along the Cameroon Volcanic Line (CVL; Figure 1b) in west Africa lacks the age progression associated with a classic mantle plume (Montigny et al., 2004), and has been explained instead by several alternative mechanisms: shear zone reactivation, small-scale convection, and lithospheric delamination (e.g., Fairhead & Binks, 1991; King & Ritsema, 2000; Reusch et al., 2010, 2011; Gallacher & Bastow, 2012; Milelli et al., 2012; De Plaen et al., 2014).

Previous observations of the X beneath Africa have been limited to a few widely scattered SS precursor observations (Deuss & Woodhouse, 2002) and localized scatterers in regional P'P'$_{df}$ precursors studies (Xu et al., 1998) and P-to-S receiver functions (RFs) (Owens et al., 2000; Rein et al., 2020; Pugh et al., 2021). Such point observations do not span competing models of hotspot tectonism, limiting their ability to interrogate the causal mechanisms of the X in the upper mantle. A detailed, continent-wide study of the X is required to understand its exact geographical distribution and the mechanisms that lead to observation. Using seismic network data that sit atop sites of African mantle upwellings, Cenozoic magmatism, and cratonic lithosphere, we map the presence of the X-discontinuity beneath the African continent using receiver functions.

1.2 African Cenozoic Magmatism

Cenozoic magmatism across the African continent has been linked to multiple mantle upwellings of varying scale, geodynamic causal mechanism and thermochemical na-

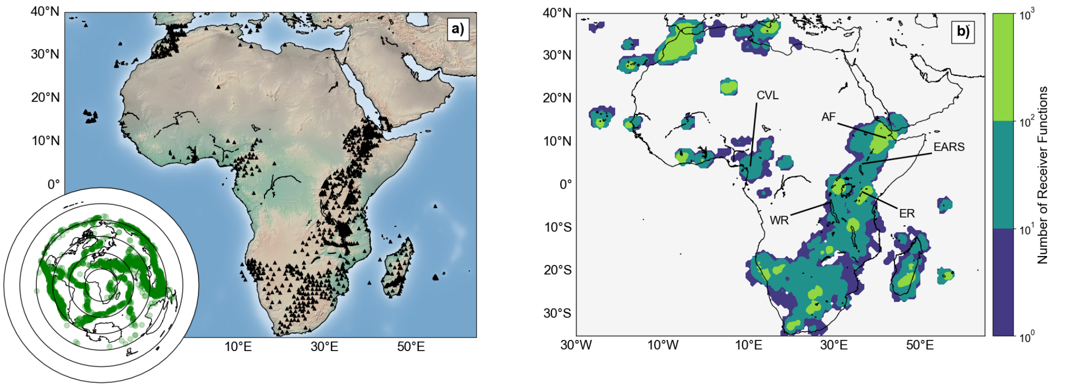

Figure 1. a) Station distribution (black triangles) across Africa and its surrounding islands. The inset globe shows the earthquake distribution (green circles) for this study and black circles represent distance intervals of 30° at 30–180° epicentral distance from the centre of Africa. b) Receiver function distribution across Africa for piercepoints of P300s at 300 km depth using raypaths through PREM (Dziewonski & Anderson, 1981) calculated using the TauP toolkit (Crotwell et al., 1999). AF: Afar, CVL: Cameroon Volcanic Line, EARS: East African Rift System, ER: Eastern Rift, WR: Western Rift.

ture. Uplifted plateaux in northeast, central and southern Africa (Lithgow-Bertelloni & Silver, 1998) and the 45 Ma Ethiopian flood basalts (e.g., Furman et al., 2006; Rooney, 2017) have been associated with ongoing rift-related magmatism along the EARS. One or more mantle upwellings have been invoked to explain uplift, elevated ^{3}He/^{4}He anomalies, the surface distribution of magmatism, and the observed mantle transition zone structure (Ebinger & Sleep, 1998; Furman et al., 2006; Pik et al., 2006; Rooney, 2017; de Gouveia et al., 2018; Chang et al., 2020; Boyce & Cottaar, 2021). Global tomographic models reveal a broad, low-wavespeed anomaly extending from the core-mantle boundary beneath southern Africa to the surface below the EARS (Ritsema et al., 1999, 2010; Chang et al., 2015; French & Romanowicz, 2015). Some continental to regional scale models decompose this broad anomaly into multiple smaller low-wavespeed anomalies in East Africa linked to mantle plume activity (Emry et al., 2019; Chang et al., 2020; Boyce et al., 2021). However, the exact number of upwellings is debated with up to three being proposed to explain surface magmatism (Chang et al., 2020) and further suggestions that these could comprise multiple smaller-scale upwellings in the upper mantle (Furman et al., 2006; I. Bastow et al., 2008; Civiero et al., 2015, 2016).

The linear trend of Cenozoic magmatism across Morocco has previously been attributed to edge-driven convection (King & Anderson, 1998; King & Ritsema, 2000; Missenard & Cadoux, 2011; Kaislaniemi & van Hunen, 2014), delamination of the root of the Atlas mountains (Bezada et al., 2014) and diversion of the Canarian mantle plume (Duggen et al., 2009; Mériaux et al., 2015; Miller et al., 2015). Whilst several tomographic models suggest the Canaries sit atop a whole mantle plume (French & Romanowicz, 2015; Marignier et al., 2020), geochemical evidence suggests that Moroccan and Canarian magmatism do not share a single deep origin and are attributable to several upper mantle upwellings (Lustrino & Wilson, 2007; van den Bogaard, 2013). However, recent tomographic models show these upper mantle upwellings are connected at depth (Civiero et al., 2018), with upwelling beneath the Azores and Cape Verde also connected to the same common deep source (Saki et al., 2015).

The CVL in west Africa is a linear chain of volcanoes oriented NE/SW including four islands offshore in the Gulf of Guinea (Fitton, 1980; Déruelle et al., 1991). Despite being observed in at least one global tomographic model (e.g., French & Romanowicz, 2015), the robustness of a whole mantle plume beneath Cameroon in tomographic models is debated (Emry et al., 2019; Marignier et al., 2020; Boyce et al., 2021). With no age progression to magmatism along the CVL (Montigny et al., 2004), several alternative mechanisms have been invoked to explain magmatism including edge-driven convection (King & Anderson, 1998; King & Ritsema, 2000; Reusch et al., 2010, 2011), lithospheric delamination and/or fault zone reactivation (e.g., Milelli et al., 2012; De Plaen et al., 2014; Fairhead & Binks, 1991; Gallacher & Bastow, 2012), and lateral flow of plume material from East Africa (Ebinger & Sleep, 1998).

In central Madagascar, magmatism has been linked with uplift, lithospheric thinning and intercontinental extension (Melluso et al., 2016; Cucciniello et al., 2017). An alternative view connects central Madagascan magmatism to lateral flow of plume material from East Africa as suggested beneath Comoros and northern Madagascar (Ebinger & Sleep, 1998). Recent seismological studies find a thin mantle transition zone (MTZ) beneath south and central Madagascar (Boyce & Cottaar, 2021) and low wavespeed anomalies extending to the lower mantle (Boyce et al., 2021; Tsekhmistrenko et al., 2021), suggesting the presence of a thermal upwelling in this region. In nearby Réunion, magmatism has been shown to be underlain by a mantle plume from seismic tomography (French

& Romanowicz, 2015; Tsekhmistrenko et al., 2021) and anomalously high $^3He/^4He$ ratios (Graham et al., 1990).

2 Data and Method

2.1 Data

We extend the receiver function (RF) data sets of Boyce and Cottaar (2021) and Pugh et al. (2021) using data recorded up until October 2021 downloaded from the Incorporated Research Institutions for Seismology (IRIS) Data Management System for teleseismic earthquakes with magnitude (M_W) $\geq$ 5.5 at epicentral distances of 40-90°. We capitalize on the new TRAILS data set in the Turkana Depression (I. D. Bastow, 2019; Ebinger, 2018; Kounoudis et al., 2021), and a further data set in northeast Uganda (Nyblade, 2017) where there is a paucity of station coverage in our RF data set along the East African Rift (EAR). This results in $\sim$200,000 event-station pairs recorded between January 1990 and October 2021, recorded at >1,800 stations. The distribution of stations and events is displayed in Figure 1a and a full list of networks used in this study can be found in the Open Research Section and Table S1.

2.2 Receiver Functions

We use P wave RFs to highlight P to S converted phases (Pds; where d denotes the depth of conversion) from the upper mantle. Pds converted from the X are herein referred to as PXs. SV waves converted from an incident P wave are radially polarized. RF analysis (Langston, 1979) constitutes deconvolution of the vertical component seismogram from the radial component assuming that the vertical component represents a convolution of the earthquake source, instrument response and some noise. Subsequently the RFs can be stacked to emphasize the low-amplitude Pds arrivals. RFs record the discontinuity structure at depth near a seismometer. We use the iterative, time-domain deconvolution method (Ligorria & Ammon, 1999) to construct RFs, which iteratively adds Gaussian pulses to reduce the least squares misfit between the predicted and observed radial seismograms. Traces are windowed 25 s before and 150 s after the P-wave to include depth phases in the source deconvolution and remove correlated noise between the vertical and radial traces. Data are bandpass filtered with corner frequencies 0.01 and 0.4 Hz, isolating the frequency band with the largest X amplitudes (Pugh et al., 2021).

Approximately 10% of RFs remain after automatic quality control (see Pugh et al., 2021, for details), leaving 20,630 RFs. Of these, 18,017 remain after further manual inspection to remove obvious low quality RFs (Section S3 and Figure S1a).

RF are initially converted from time-to-depth using the 1D velocity model PREM (Dziewonski & Anderson, 1981). However, 1D time-to-depth conversions can result in >20 km of error on upper mantle discontinuities (Pugh et al., 2021). To perform 3D velocity corrections SEMUCB_WM1 (French & Romanowicz, 2014), and a recent model of the African continent, AF2019 (Celli, Lebedev, Schaeffer, & Gaina, 2020), are used. While tomographic models suffer from sparse and uneven data coverage beneath Africa, the resolution should be greatest where receiver functions are located. This condition is valid especially for the recent model of Celli, Lebedev, Schaeffer, and Gaina (2020), which incorporates body waves from recently available seismic arrays.

2.3 Stacking and Vote Mapping

The amplitudes of Pds on individual RFs are <10% of the incoming P wave and will typically be lower than the noise on an individual trace. As such, high-quality RFs with overlapping sensitivity in upper mantle are stacked to amplify coherent Pds and suppress noise. Following the spiral distribution of Rakhmanov et al. (1994), equidistant bins of radius 111 km (∼1° at the equator) are defined across the globe overlapping by ∼0.5°. All RFs that traverse the upper mantle within a bin, estimated using their ray theoretical pierce point at 300 km depth from the TauP toolkit (Crotwell et al., 1999), are stacked together in the depth and time-slowness domains (see Pugh et al., 2021, for details). Visual inspection shows that the majority of stacks with <30 RFs are of poor quality. Therefore, stacks containing >30 RFs are assessed by the visibility of Pds phases in slowness stacks as outlined in Pugh et al. (2021) to determine robust (Figure 2a and b), potential (Figure 2c and d) and null (Figure 2e and f) observations of the X-discontinuity.

Common conversion point stacking (Dueker & Sheehan, 1997) has previously been used to map the 410 km and 660 km discontinuities across Africa, as well as the presence of mid-mantle discontinuities (Thompson et al., 2015; Reed et al., 2016; Boyce & Cottaar, 2021). This technique relies on stacking all depth converted RFs that traverse the upper mantle within a defined Fresnel zone width at each point in a regular grid. Whilst this provides a powerful tool for analyzing these surfaces, slowness information is not con-

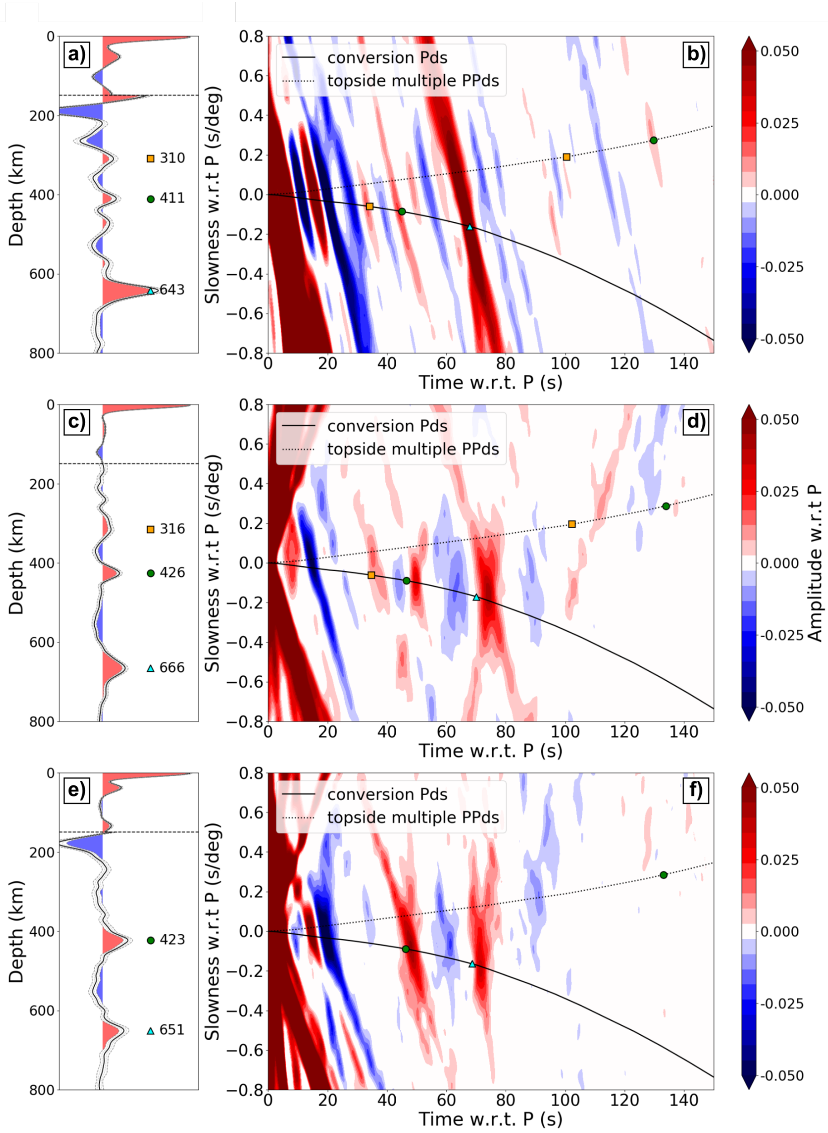

Figure 2. Example stacks for X-discontinuity classifications of Robust (a and b), Potential (c and d) and Null (e and f) respectively. Depth (a, c and e) and slowness stacks (b, d and f) with 130, 370 and 137 RFs, filtered at 0.01–0.4 Hz. Depth stacks (a, c and e): Time-to-depth converted RFs are linearly stacked with the black line marking amplitude (normalized to P) and dashed lines marking 2 σ_M. Amplitudes are multiplied by 5 below the horizontal dashed line at 150 km depth. Stacks are converted from time-to-depth using SEMUCB_WM1. Colored symbols mark significant peaks from PXs (orange squares), P410s (green circles), and P660s (cyan triangles). Slowness stacks (b, d and f): RFs with amplitude >2 σ_M normalized to P stacked in the time-slowness domain. Predicted time-slowness curves are shown for the direct (Pds) and multiple (PPvds) phases. The colored symbols correspond to predicted times and slownesses for direct arrivals and PPvds multiples for significant arrivals in the depth stacks computed from PREM.

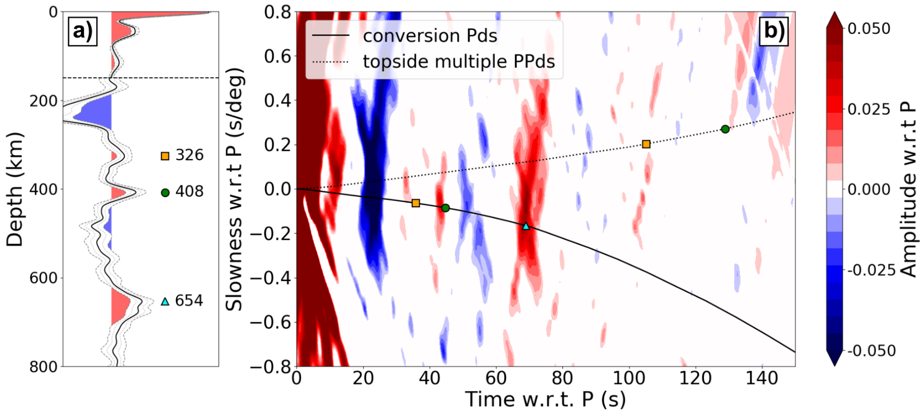

Figure 3. Example of a contaminating PPvds multiple. Depth (a) and slowness stack (b) for 31 RF, filtered at 0.01–0.4 Hz. Depth stack: Time-to-depth converted RFs are linearly stacked with the black line marking amplitude (normalized to P) and dashed lines marking 2 σ_M. Amplitudes are multiplied by 5 below the horizontal dashed line at 150 km depth. The stack is converted from time-to-depth using SEMUCB_WM1. Colored symbols mark significant peaks from PXs (orange squares), P410s (green circles), and P660s (cyan triangles). Slowness stack: RFs with amplitude >2 σ_M normalized to P stacked in the time-slowness domain. Predicted time-slowness curves are shown for the direct (Pds) and multiple (PPvds) phases. The colored symbols correspond to predicted times and slownesses for direct arrivals and PPvds multiples for significant arrivals in the depth stacks computed from PREM.

sidered. With the presence of shallow upper mantle PPvds phases contaminating the depth and slowness interval considered for the X (e.g., Figure 3), common conversion point stacking is deemed unsuitable.

Here, a vote mapping procedure (e.g., Lekic et al., 2012) is carried out whereby each bin that intersects a 0.5°× 0.5° region counts a "vote" towards that region, with robust, potential and null bins voting +1, 0, or -1 to that region respectively. Regions with ≥2 votes in Figure 4 are normalized by the number of votes to account for a heterogeneous data coverage. Regions with <2 votes are masked. We interpret the resulting smooth map as an increasing likelihood that an X is present (positive values) or not present (negative values). Using this approach of a vote map with overlapping bins reduces the dependence of our results on a specific choice of grid. Whilst the depth information of common conversion point stacking is lost, this provides a robust representation of the dis-

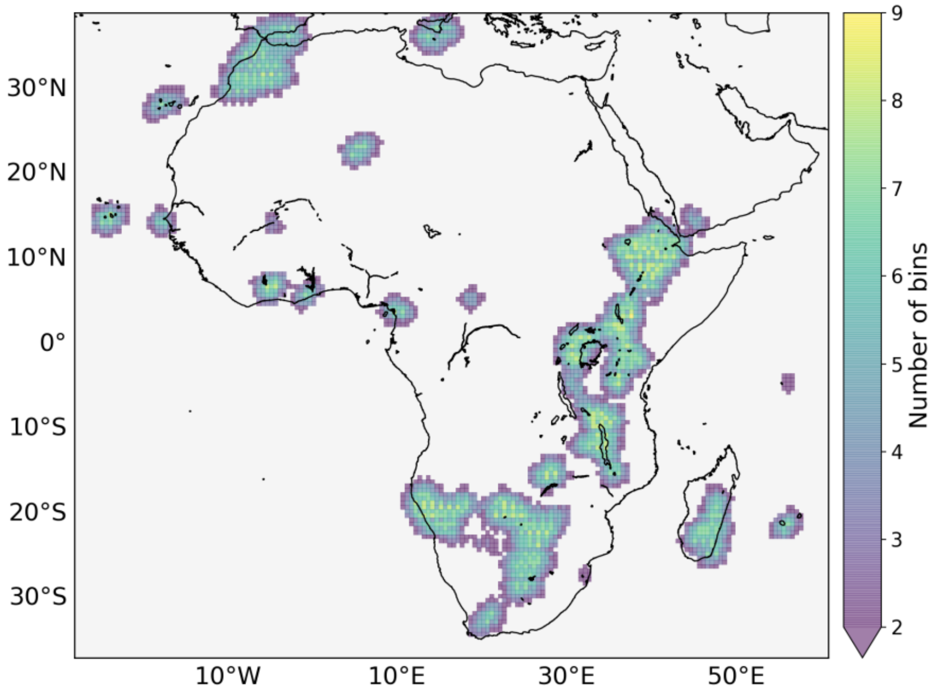

Figure 4. Number of 1° radius bins intersecting each 0.5° × 0.5° bin for normalized vote mapping.

tribution of the X and its potential length scales across the continent including depth and slowness information.

3 Results

3.1 Geographical distribution of the X-discontinuity

The upper mantle beneath the African continent is imaged using >18,000 RFs. Depth and slowness stacks are computed to identify observations of the X for nearly 600 overlapping bins of 1° radius. Using a normalized vote mapping approach in Figure 5, the geographical distribution and length-scales of the X-discontinuity are displayed across the African continent. X observations cluster around the Canaries, Cameroon, Cape Verde, Ethiopia, the Hoggar volcanic province, southernmost Madagascar, Morocco, and Reunion with intermittent observations appearing along the Western Rift (WR). Null observations are prevalent in southern Africa, along the Eastern Rift (ER), and in north-

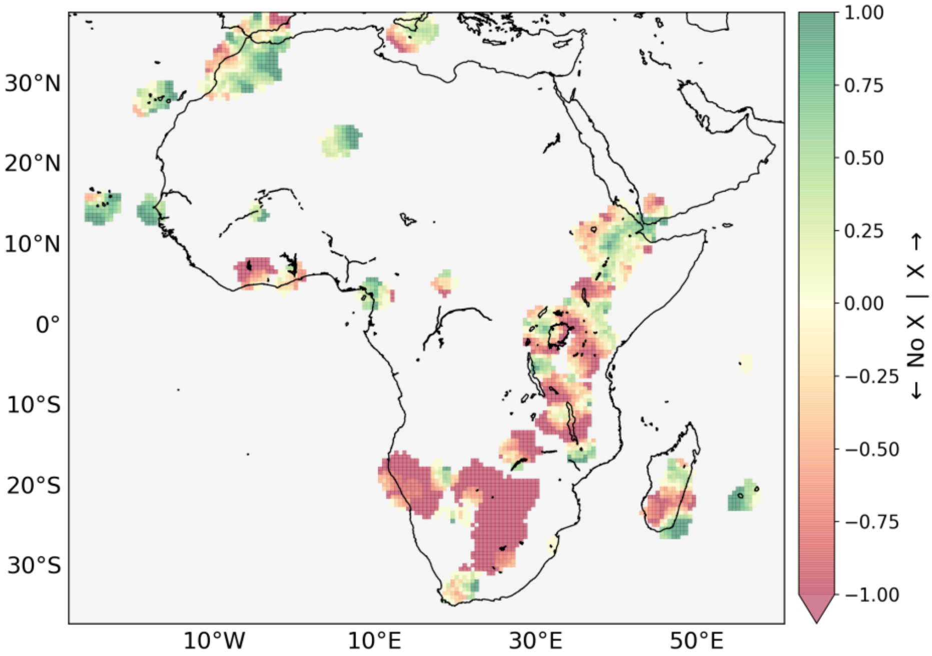

Figure 5. Normalized vote map of X-discontinuity observations for 597 overlapping 1° radius bins with ≥2 votes on a 0.5°× 0.5° grid with darkening green colours showing an increasing likelihood of the X and darkening red colours showing an increasing likelihood of no X. Votes are based upon the presence of the X-discontinuity in slowness stacks.

ern Madagascar. This distribution is explored further in the context of magmatism in Section 4.2.

The number of RFs in a stack has little bearing on its classification (Figure S2). However, the backazimuth distribution of RFs has a strong control on epicentral distance distribution, thus determining the streakiness of slowness stacks and potentially masking X observations (Figure S4; Section S4).

3.2 Depth distribution of the X-discontinuity

Nearly 600 depth and slowness stacks with > 30 RFs are visually inspected for the presence of the X-discontinuity. Upper mantle positive conversions are present in the depth range of 212–377 km, 233–340 km, and 235–347 km depth for 262 stacks using PREM, SEMUCB_WM1 and AF2019, respectively. Using the criteria set out in Pugh et al. (2021), 172 stacks are classed as robust with the correct slowness for PXs, 121 stacks are classed as potential, 303 stacks are classed as null and only one stack is classed as poor quality; 59 stacks contain robust observations of PPvXs.

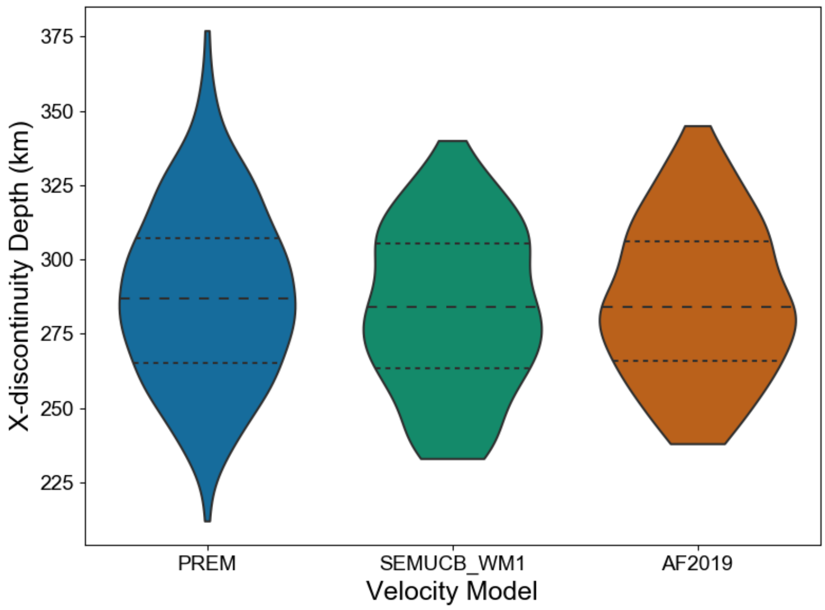

Figure 6. Violin plots of X-discontinuity depths observed in depth stacks cut to the minimum and maximum observations for the three velocity models used in this study: PREM, SEMUCB_WM1 and AF2019. Dashed lines mark the 1^{st}, 2^{nd} and 3^{rd} quartiles of each violin.

Including slowness information, robust X-discontinuity depths range between 233 and 340 km, centered around a mean depth of 284 km with lower and upper quartiles of 264 and 305 km respectively for SEMUCB_WM1 (Figure 6). Though the total data distribution shifts deeper when using AF2019 (238-345 km depth), the mean depth and quartiles (284 km, 266 km and 306 km) are remarkably similar to those from SEMUCB_WM1.

SEMUCB_WM1 is preferred for depth correction as temperature variation and topography calculated in Section S5 suggest it better accounts for upper mantle velocity structure. Subsequently, depths reported below are as converted using SEMUCB_WM1 and displayed in Figure 7.

Only 34% of the depth and slowness stacks that contain PXs also contain PPvXs arrivals. It is logical that the percentage of stacks containing PPvXs is lower beneath the continents than the 60% percent in Pugh et al. (2021), where stacks are predominantly made beneath ocean islands. The heterogeneous nature of the continental crust

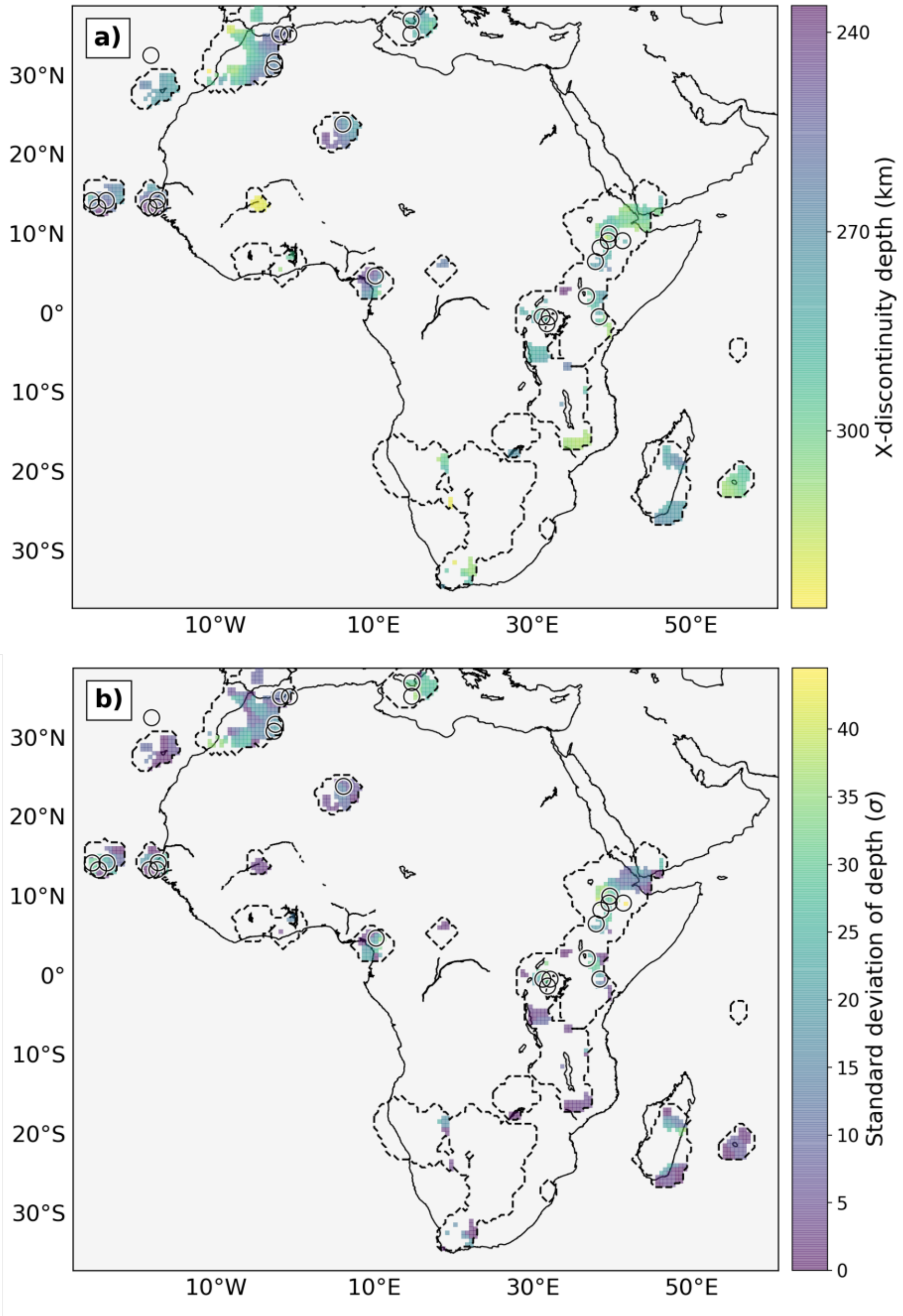

Figure 7. Vote maps of a) X depth and b) standard deviation of depths (σ) for 597 overlapping 1° radius bins with ≥2 votes, and an average vote ≥ 0.25 (Figure 5), on a 0.5° × 0.5° grid. Black circles mark bins where two X observations are made and black dashed contours mark the enter of the vote map (Figures 4 and 5).

and lithosphere may inhibit coherent stacking of PPvXs, especially considering the greater/variable thickness of the continental lithosphere.

4 Discussion

4.1 Potential trends in the X-discontinuity

We explored discontinuities in the upper mantle beneath the African continent and surrounding ocean islands in ∼600 equally spaced depth and slowness stacks (Figure 8). Scattered observations of the X exist in nearly 30% of the stacks over a broad depth range of 233–340 km. Figure 8a shows that the depth and amplitude distribution of these results is comparable to those in Pugh et al. (2021) with the largest amplitudes of ≥8% of the main P wave arrival found at ∼280 km depth and smaller amplitudes of ≤3% below 330 km depth. No clear correlation exists between the depth of the X and its amplitude (Figure 8a). We calculate average upper mantle temperatures at 200–400 km depth for every stack at ±1° latitude and longitude using the temperature deviations found in the geophysical-petrological inversion of Fullea et al. (2021). No correlation can be found between the depth of the observed X and these local thermal perturbations (Figure 8b) and the X is no more readily observed at elevated upper mantle temperatures than at depressed temperatures (Figure S6). However, null observations of the X are more readily found at depressed mantle temperatures (Figure S6). Without a trend in the temperature-depth space, it is impossible to infer a Clapeyron slope for the X. With no Clapeyron slope, and such a broad range in depths and amplitudes, we conclude multiple causal mechanisms are responsible for the X below continents.

X discontinuity observations are broadly found beneath the thinnest lithosphere across the African continent (Figure S7) using three global tomographic models (Schaeffer & Lebedev, 2013; Debayle et al., 2016; Priestley et al., 2018). X observations closely track the thin lithosphere of the Main Ethiopian Rift and are present beneath several ocean islands. However, the X is absent beneath thick cratonic lithosphere. One explanation for the lack of X observations below thick lithosphere concerns multiples. PPvds multiples are expected to arrive at seismic stations at the same time as PXs conversions when d ≈ 80–100 km, similar to the depth of the mid-lithospheric discontinuities reported in S wave RF studies beneath the Tanzanian (Wölbern et al., 2012) and Kalahari (Sodoudi et al., 2013) cratons, though these discontinuities are observed with the opposite polar-

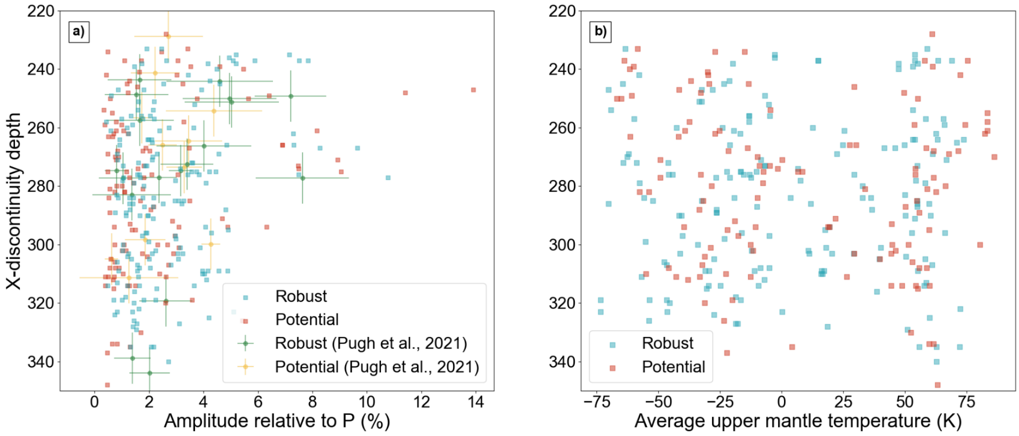

Figure 8. a) Depth and amplitude distribution of 172 robust X-discontinuity observations, and 121 potential X-discontinuity observations plotted alongside the observations of Pugh et al. (2021). Depths are converted using SEMUCB_WM1. Error bars are calculated in depth and amplitude using 10 jackknife resamples with 90% of the data in each sample. Amplitude error bars represent $\pm 2\ \sigma_M$ of the mean of each stack whereas depth error bars represent the mean width of the PXs $+2\ \sigma_M$ peak at the PXs amplitude across all stacks. Error bars are not displayed for observations from this study to avoid overcrowding the axes. b) Depth and average upper mantle temperature distribution of 172 robust X-discontinuity observations, and 121 potential X-discontinuity observations. Temperatures deviations are taken from Fullea et al. (2021) and averaged at 200–400 km depth.

ity to the X. As for the lithosphere-asthenosphere boundary, only 13–21% of 0.5° × 0.5° bins in our vote map sample lithosphere between 80 and 100 km thick according to maps derived by Hoggard et al. (2020) using velocity models SLNAAFSA (Schaeffer & Lebedev, 2013, 2014; Celli, Lebedev, Schaeffer, & Gaina, 2020; Celli, Lebedev, Schaeffer, Ravenna, & Gaina, 2020), CAM2016 (Ho et al., 2016; Priestley et al., 2018) and 3D2015-sv (Debayle et al., 2016). As such, interfering phases are unlikely to be a persistent issue for RF stacks. While thick heterogeneous lithosphere could result in the incoherent stacking of RFs, very low standard error in null stacks beneath cratons suggests that, for the thickest lithosphere, this does not occur.

In line with our correlation between null observations and depressed upper mantle temperatures, we suggest a cooler asthenospheric mantle underlying thicker lithosphere may present unfavorable conditions of X formation/visibility. This is, however, challenging to prove with our results alone. For stacks classed as potential, limited backazimuth and epicentral distance distribution resulting in streaky slowness stacks seems to have the largest control on the X observation robustness (Section S4).

While no quantitative relationship is found between the depth of the observed X and estimated temperatures in the upper mantle, most regions of Quaternary-recent magmatism are associated with an X observation: they are located proximally to several ocean islands (Canaries, Cape Verde, Réunion), Morocco, Cameroon, the East Africa Rift and Madagascar, and overlap with our previous RF stacks (Pugh et al., 2021). While robust X observations were found in the Canaries and Cameroon in Pugh et al. (2021), this current study highlights the importance of studying the X over short wavelengths with potential observations in Cape Verde, Hoggar, Afar and Réunion now found to be robust. The non-robustness of X signals in these regions in Pugh et al. (2021) may have been the result of unimodal backazimuth and epicentral distance distributions causing streaky slowness stacks (e.g., Figure S4) or topography across the X on short wavelengths as can be seen for Cape Verde, Hoggar and Réunion (Figure 7). These locations all host Quaternary volcanoes and/or Cenozoic magmatism (Figure 9). Alongside X observations in regions of ongoing subduction (e.g., Revenaugh & Jordan, 1991; Schmerr et al., 2013), these observations suggest the X to be related to recent upwelling or downwelling, with chemical heterogeneity mixed into the mantle during subsequent mantle convection. The causal mechanisms and implications of these observations are discussed below to explore the cause of the X-discontinuity across upwellings of variable geodynamic origin.

4.2 Links to Surface and Geodynamic Features

4.2.1 East Africa

The presence of the X beneath East Africa may be related to chemical heterogeneity introduced by mantle upwellings in the region (Simmons et al., 2007; Rooney, 2017; Boyce & Cottaar, 2021). Robust X observations underlie several sections of the EARS from Afar in the north, through Ethiopia and two patches beneath the WR, to a small patch in Mozambique at depths of 270-320 km (Figure 10a). Notable null results are seen beneath the Turkana Depression, along the ER, and under the Tanzanian craton where substantial volumes of data exist. In Ethiopia, X depths gradually increase northwards to Afar (Figure 11). If the X is controlled by a common causal mechanism beneath the

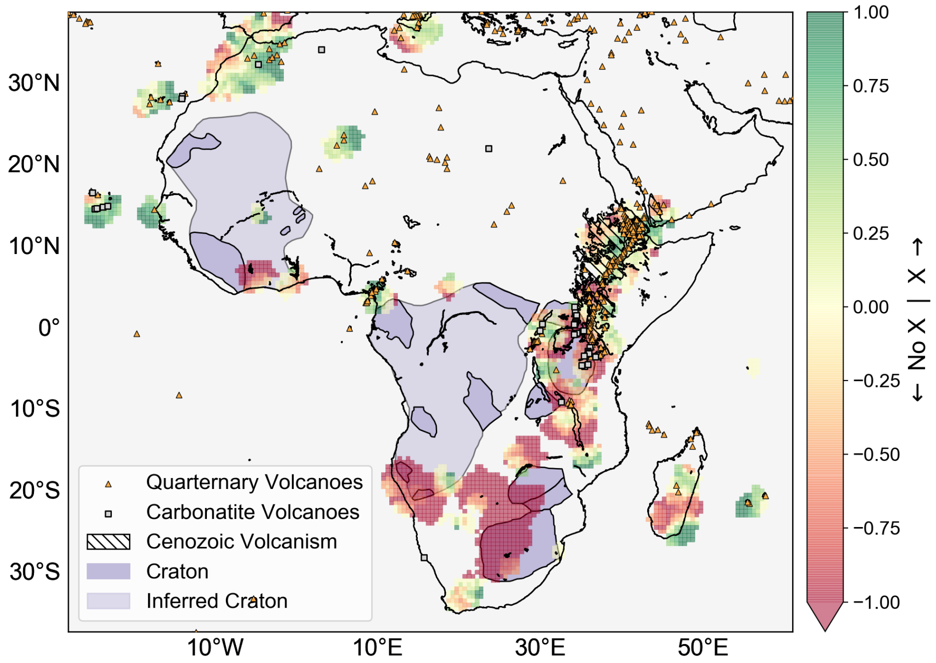

Figure 9. X-discontinuity vote map (Figure 5) plotted above cratons and Cenozoic magmatism adapted from (Begg et al., 2009; Boyce et al., 2021; Kounoudis et al., 2021). Carbonatite volcanoes plotted are ∼45 Ma-recent (Woolley & Kjarsgaard, 2008; Muirhead et al., 2020).

EARS, the positive Clapeyron slope of the Co-St (Akaogi et al., 2011) would suggest an increase in temperature towards Afar, consistent with reductions in seismic wavespeed (Boyce et al., 2021). However, the impact of the variable presence of melt on seismic wavespeeds makes isolating thermal controls on seismic heterogeneity difficult to isolate (e.g., Rooney et al., 2012; I. Bastow et al., 2008).

There is significant debate as to the number of plumes that exist in the upper mantle in East Africa and whether they are commonly or uniquely sourced. One to three whole-mantle plumes of variable thermochemical nature or multiple upper mantle plume heads have been proposed to explain surface magmatism on the strength of seismological and geochemical evidence (Ebinger & Sleep, 1998; Furman et al., 2006; Pik et al., 2006; Civiero et al., 2015, 2016; de Gouveia et al., 2018; Chang et al., 2020; Boyce & Cottaar, 2021). Robust X observations closely follow the Main Ethiopian Rift from Afar to southern Ethiopia, and reappear along parts of the western rift marked by Quaternary volcanism (Figures

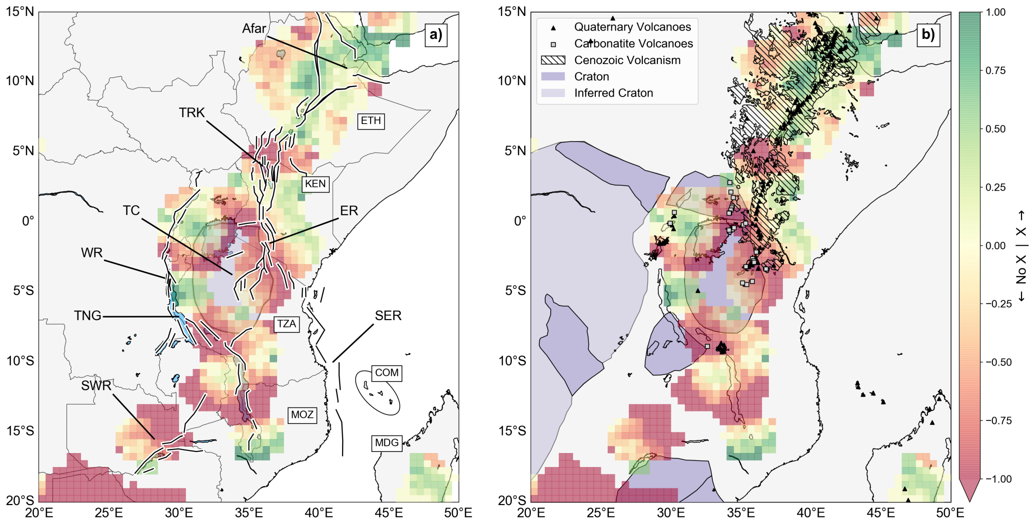

Figure 10. a) X-discontinuity vote map (Figure 5) plotted above the Tanzanian Craton (TC - purple) and lakes (blue) along the EARS (TRK, Lake Turkana; TNG, Lake Tanganyika). Major faults adapted from Jones (2020) are marked with thick black and white lines and reveal the Eastern, Western, Southeastern and Southwestern rifts (ER, WR, SER, SWR). National borders are marked with thin black lines and countries referred to in text are labelled (COM, Comoros Archipelago including Mayotte; ETH, Ethiopia; KEN, Kenya; MDG, Madagascar; MOZ, Mozambique; TZA, Tanzania). b) X-discontinuity vote map (Figure 5) plotted above cratons and Cenozoic magmatism adapted from (Begg et al., 2009; Boyce et al., 2021; Kounoudis et al., 2021). Carbonatite volcanoes plotted are ∼45 Ma-recent (Woolley & Kjarsgaard, 2008; Muirhead et al., 2020).

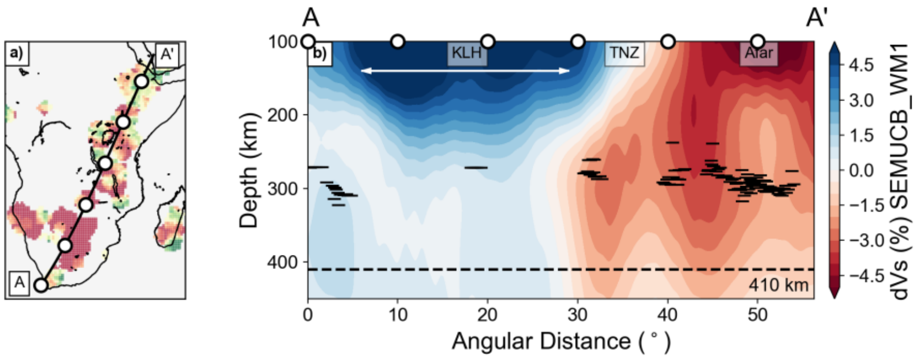

Figure 11. Along profile a), a cross-section b) of X-discontinuity depths of robust observations from South Africa to Afar plotted above the tomographic model SEMUCB_WM1 (French & Romanowicz, 2015). X-discontinuity depths are taken from bins in Figure 7 ≤250 km from the line of section. KLH, Kalahari Craton; TNZ, Tanzanian Craton. The white arrow marks the horizontal extent of the Kalahari Craton.

10). Widely distributed X observations suggest chemical heterogeneity is pervasive throughout East Africa around 300 km depth and so presents no clear support for multiple small scale upwellings that have been reported by some workers (Civiero et al., 2015, 2016) or underlying plumes of variable thermochemical nature (Boyce & Cottaar, 2021), at least at X depths. We therefore broadly support the notion that plume signatures in the East African upper mantle are well mixed and the upper mantle pervasively hosts material transported from depth by the African Superplume (e.g., Rooney, 2017). However, we note that some scatter in X observations in East Africa may be associated with the variable presence of CO_2 assisted silicate melting that is required to explain the discrepancy between mantle potential temperature estimates and slow seismic wavespeeds below depths commonly associated with decompression melting (Rooney et al., 2012). Previous workers show the basal impedance contrast from such a carbonate silicate melt layer presents a viable explanation for the X (Dasgupta et al., 2013).

Moving southwards from Ethiopia, X observations terminate abruptly north of Lake Turkana (Figure 10) forming a WNW–ESE band of null observations that interrupt the broad trend of robust observations below the East African Rift. Given the presence of Quaternary volcanoes and Cenozoic magmatism in much of the Turkana Depression (Figure 9), this result may indicate a locally different geodynamic environment to that observed below the Ethiopian and East African plateaus beneath which two separate plumes have been proposed (e.g., Pik et al., 2006). However, recent tomographic models present no clear evidence for a break in slow wavespeeds (and therefore dynamic support) at the upper mantle depths to which our data are sensitive (Hansen et al., 2012; Emry et al., 2019; Celli, Lebedev, Schaeffer, & Gaina, 2020; Boyce et al., 2021; Kounoudis et al., 2021). Intriguingly, a fast wavespeed band at lithospheric depths in southernmost Ethiopia in the seismic tomographic study of Kounoudis et al. (2021), coincident with a broadly (∼500 km-wide) rifted zone (Figure 10) co-exists with our zone of absent X. This anomalous region, interpreted by Kounoudis et al. (2021) as refractory Proterozoic lithosphere, is not associated with Quaternary volcanism, perhaps resulting in a lack of melt ponding below the region at X depths. Complex lithospheric seismic structure, both associated with the Kounoudis et al. (2021) fast wavespeed band, and with the failed Mesozoic Anza rift immediately to the south of it in the Turkana Depression, may be precluding our view of the X.

South of the Turkana Depression, the EARS splits into the ER, WR, Southwestern and Southeastern rift zones (Figure 10a), which developed in Proterozoic lithosphere between thick cratonic lithosphere (e.g., Chorowicz, 2005; Mulibo & Nyblade, 2016; Ebinger et al., 2017; Daly et al., 2020). Owens et al. (2000) observe Pds arrivals at 250–300 km across Tanzania, but they note that they cannot discriminate between a Pds phase or a shallower multiple from velocity analysis alone. This region overlaps with regions of X observations east of Lake Tanganyika along the WR and null observations due east along the ER. Unlike the ER that has experienced 30 Ma-Recent magmatism along its length, the WR is characterized by isolated, volumetrically small magmatic provinces (e.g., Ebinger, 1989; Chorowicz, 2005; Roberts et al., 2012). The Southwestern rift zone has no known magmatism, whereas the Southeastern rift zone offshore between Africa and Madagascar has experienced ∼20 Ma-recent magmatism (e.g., Michon, 2015; Courgeon et al., 2016, 2017; O'Connor et al., 2019; Berthod et al., 2022). Therefore, it is striking that the ER is underlain by null X observations while patchy X observations underlie the WR (Figure 9a). The two patches along the WR show consistent X depths of ∼290 km, however, at the surface, the northern patch is colocated with carbonatite magmatism while the southern patch underlies no surface magmatism. Furthermore, the role of the Tanzanian Craton, separating the two branches remains enigmatic. Whether through edge-driven convection (King & Anderson, 1998; King & Ritsema, 2000) or lateral diversion of plume material around the cratonic keel as suggested beneath the Kalahari Craton (Forte et al., 2010; Tepp et al., 2018), it remains uncertain whether the Tanzanian Craton could divert chemically heterogeneous plume material to the WR. However, the Tanzanian Craton has a shallower depth extent than other cratons globally (e.g., Priestley et al., 2018; Celli, Lebedev, Schaeffer, & Gaina, 2020). Consequently, it is unclear whether it would have a similar impact on upper mantle flow compared to cratons of typical thicknesses ($\geq$250 km). Whether craton induced flow would result in our null observation beneath the ER is also elusive.

4.2.2 Canaries

Robust X observations occur at 270–280 km depth beneath the Canaries (Figure 7a) with the most robust results appearing to the north and east (Figure 5). The Canaries have been shown to overlie a whole mantle plume in tomographic models (French & Romanowicz, 2015; Marignier et al., 2020), meaning, similarly to East Africa, the X beneath the Canaries may also result from the introduction of chemical heterogeneity from the deep mantle. Canarian shield stage lavas contain the signatures of both old (>1 Ga; Thirlwall, 1997; Gurenko et al., 2006, 2009) and young (<1 Ga; Widom et al., 1999; Geldmacher & Hoernle, 2000) recycled oceanic crust. Should the Canarian mantle plume recycle oceanic crust to the surface, this may provide necessary chemical heterogeneity to explain the X via a single causal mechanism here, similar to other ocean island hotspots (e.g. Kemp et al., 2019; Pugh et al., 2021).

4.2.3 Morocco

The X is widespread beneath Morocco. Observations of the X at 250–310 km depth (Figure 7a) show the greatest variation in depth over short spatial distances for our study region. Here the X has been observed in several previous studies (e.g. Deuss & Woodhouse, 2002; Rein et al., 2020), with potential links to the Canaries mantle plume (e.g. Rein et al., 2020). We observed the X at depths of $\sim$310 km on the western coastline shallowing monotonically eastwards to $\sim$250 km (Figure 7a). However, to the south of this region, Rein et al. (2020) observe the X deepening $\sim$eastwards from $\sim$310 km to $\sim$350 km. Considering the Clapeyron slope of the Co-St phase transition invoked by Rein et al. (2020), it would be expected to deepen with increasing temperature. Wavespeed anomalies in this region in SEMUCB_WM1 and AF2019 transition from slow in the west, to fast in the east. Interpreted in terms of temperature, this would suggest a cooling trend west to east, and a shallowing X in line with our observations. Double X observations observed in this region (Deuss & Woodhouse, 2002; Rein et al., 2020) may explain discrepancy with our shallowing results. Although we do not observe two X observations, there is a large standard deviation in X depth between stacks (Figure 7b). Large standard deviation in depth is a reasonable indicator that two X observations may occur, often being colocated with two X observations elsewhere in the African continent (Figure 7), though the secondary arrival may be a multiple.

Duggen et al. (2009) present geochemical analyses to show that the Canaries plume may have deflected to the northeast beneath the Moroccan lithosphere, a suggestion supported by plume modelling (Mériaux et al., 2015). However, several studies (Lustrino & Wilson, 2007; van den Bogaard, 2013) show that the geochemistry of magmatism across the region does not fit with a single origin deep sourced mantle plume and is more readily reconciled by multiple upper mantle upwellings. This remains a topic of ongoing debate with a recent regional tomographic study suggesting that these multiple upwellings may have a common deep source (Civiero et al., 2018). Rein et al. (2020) use evidence of old and young recycled oceanic crust in lava samples from the Canaries (e.g., Thirlwall, 1997; Gurenko et al., 2006, 2009), and the proximity of subducted slabs in the Mediterranean, to conclude that multiple upwellings recycle basalt into the upper mantle, facilitating the Co-St phase transition as the causal mechanism for the X. From our extended data set, it is possible that recycling of basalt may be pervasive across this region, extending offshore of Morocco beneath the Canaries.

4.2.4 Cape Verde

Shallow X observations are found to the south of Cape Verde and offshore Senegal at 240–270 km depth, shallowing approximately north to south (Figure 7a). There are also a number of doubled X observations in this region. X observations beneath Cape Verde may be associated with hotspot magmatism and potentially also linked to the Canaries plume. Whilst French and Romanowicz (2015) classify Cape Verde as overlying a 'primary plume', Marignier et al. (2020) are less confident of a plume in this location compared with the majority of their 'primary plumes'. However, Cape Verde exhibits HIMU and EM geochemical signatures, and high $^{3}He/^{4}He$ ratios (Doucelance et al., 2003; Jackson et al., 2017, 2018), representing plume signatures. Geodynamic models (Davaille et al., 2005) and precursor studies (Saki et al., 2015) found the Cape Verde plume to have a common source in the lower mantle with the Canarian plume to the north. Should this be the case, recycled basalt may be sourced from this singular upwelling ponded below the 660 km discontinuity (e.g., Davaille et al., 2005).

4.2.5 Hoggar

We observe the X-discontinuity beneath the Hoggar mountains at 270–280 km depth, deepening to the East (Figure 7a) where we find the most robust observations (Figure 5). While the X is present beneath Hoggar, its relationship to a potential mantle plume is uncertain. In the hotspot catalogue of Courtillot et al. (2003), Hoggar has one of the lowest probabilities of being a whole mantle plume (Marignier et al., 2020) and is classified as only 'somewhat resolved' by French and Romanowicz (2015). Further, the lavas in Hoggar are characterized by MORB-like $^3He/^4He$ ratios (Pik et al., 2006; Jackson et al., 2017) suggesting that they do not have a deep mantle source. The X is much deeper than the 150 km source depth of magmatism (Liégeois et al., 2005), thus separate processes may be invoked to explain the source of chemical heterogeneity and surface magmatism with little connection between the two. With limited station coverage it is difficult to assess the lateral extent of the X, and whether this observation is limited to the Hoggar mountains alone, or whether it is connected to the widespread X observations seen in Morocco.

4.2.6 Cameroon

Beneath Cameroon, we find the X colocated with the CVL. Robust X observations are made in western Cameroon, decreasing in confidence eastwards from positive to negative normalized votes. X observations are made at 250–290 km depth.

There is much debate as to the source of magmatism along the CVL, meaning a connection between magmatism and the X is uncertain here. Despite its linear morphology and a HIMU signature consistent with a lower mantle source (Lee et al., 1994), there is no age progression of magmatism along the CVL (e.g., Montigny et al., 2004). Further, maximum $^3He/^4He$ ratios are not distinguishable from MORB ratios (Barfod et al., 1999; Jackson et al., 2017). Continental and global tomographic models resolve a lower mantle plume (e.g., French & Romanowicz, 2015), suggest that there may be some lower mantle contribution to magmatism (Emry et al., 2019; Boyce et al., 2021), or classify the likelihood of a mantle plume as 'unclear' (Marignier et al., 2020). Previous MTZ and regional tomographic studies of the CVL do find evidence of a thermal anomaly across the MTZ (Reusch et al., 2010, 2011), favoring edge-driven convection as the source of magmatism (King & Anderson, 1998; King & Ritsema, 2000). Other workers have also favored non-plume, low melt volume mechanisms for CVL development (e.g., lithospheric delamination or fault zone reactivation: Milelli et al., 2012; Gallacher & Bastow, 2012; De Plaen et al., 2014; Fairhead & Binks, 1991).

Boyce and Cottaar (2021) find complex MTZ behavior in their recent study, with reduced 410 amplitudes, 20–30 km of thinning and variable 660 km discontinuity behavior. With mechanisms of a water-rich MTZ (Buchen et al., 2018) and a high basalt fraction (sufficient for X observation; Kemp et al., 2019) available to explain a disappearing 410 km discontinuity, Boyce and Cottaar (2021) do not preclude a lower mantle contribution to magmatism along the CVL. Should such a large basalt accumulation be present atop the 410 km discontinuity, the Co-St phase transition would be a likely candidate cause of the X in this region, as seen in Hawaii (Kemp et al., 2019). However, the depth of the X is much shallower here than the 336 km reported by Kemp et al. (2019) and such large basalt fractions remain unattainable in geodynamic models (Monaco et al., 2022).

4.2.7 Madagascar

X observations are present in two distinct patches across Madagascar. South-easternmost Madagascar is underlain by robust X observations at 270-280 km depth, with a strong band of null results through central Madagascar separating a less certain region of X observations (normalized vote ≈ 0.5) to the north (Figures 5 and 7a).

Central and southern Madagascar are associated with substantial MTZ thinning and depression of both the 410 and 660 km discontinuities (Boyce & Cottaar, 2021), indicating a thermal upwelling across the MTZ. Recent tomographic studies image a low velocity anomaly extending from the surface beneath southernmost Madagascar to greater than 1000 km depth, connected to the African LLVP (Boyce et al., 2021; Tsekhmistrenko et al., 2021). Therefore, this anomaly maybe an upwelling branch of the African Superplume. An upwelling from the lowermost mantle south of Madagascar would explain the sharp transition from null to robust X observations from north to south (Figure 5), but it is unable to explain moderately certain X observations in central Madagascar that underlie magmatism with a source depth at the base of the lithosphere (≤130 km; depth Melluso et al., 2016).

Geochemical analyses of Cenozoic basalts in central Madagascar determine their provenance to be the Madagascan continental mantle, with uplift, lithospheric thinning and intercontinental rifting being the most likely processes to trigger melting (Melluso et al., 2016; Cucciniello et al., 2017). Magma has been suggested to have spread laterally as far as Madagascar from the EARS along pre-existing structures like the Davie ridge (Ebinger & Sleep, 1998; O'Connor et al., 2019). This is corroborated by plume-like signatures and age progression of volcanics in the Comoros islands (Emerick & Duncan, 1982; Deniel, 1998). Owing to a lack of resolution offshore Mozambique, these results are unable to discriminate between these two models of melt generation. It is also undetermined whether flow would be demarcated by X observations or whether this would be constrained to the uppermost mantle.

4.2.8 Mauritius and Réunion

Mauritius and Réunion present two further hotspot ocean islands underlain by an X. The X here is at 290–310 km depth, with the highest confidence southwest of Réunion and decreasing eastwards of Mauritius.

While Marignier et al. (2020) find evidence of a mantle plume to be 'unclear' in this region, French and Romanowicz (2015) find a plume to be 'clearly resolved' with high $^3He/^4He$ ratios (Graham et al., 1990) corroborating a lower mantle source. Regional seismic tomography reveals a slow wavespeed anomaly connected to the African LLVP (Tsekhmistrenko et al., 2021). Though Tsekhmistrenko et al. (2021) invoke individual blobs episodically detaching from the LLVP and subsequently ascending buoyantly, as opposed to a continuous plume conduit, this may provide a means to recycle basalt to the upper mantle in this region. Since plumes can only support a basalt fraction of 20% (Ballmer et al., 2013; Dannberg & Sobolev, 2015), ponding of eclogite has been invoked to match the seismically observable impedance contrasts of the X (Kemp et al., 2019). It is unclear how individually ascending blobs would affect the amount of basalt available to pond in the upper mantle.

4.2.9 Southern Africa

We largely observe a lack of the X in Southern Africa where the overlying lithosphere comprises several cratons. Figure 11 shows an abrupt termination of X observations at the margins of the Kalahari Craton which is characterized by high confidence null observations. As discussed before, it remains uncertain whether strong negative conversions from the base of the craton mask weaker converted phases in RFs or whether there is indeed a lack of chemical heterogeneity/necessary geodynamic conditions to observe the X beneath the thicker lithosphere extending to $\geq$200 km depth (e.g., Priestley et al., 2008; Fishwick, 2010; Adams & Nyblade, 2011).

In Pugh et al. (2021), six stacks beneath cratonic lithosphere from Canada, Brazil, Scandinavia, Siberia and Australia displayed null X observations to higher frequency than studied here, but strong negative conversions from the base of the craton still dominate the region for PXs conversions in depth and slowness stacks. Cooler than average mantle temperatures may be expected beneath the base of the cratons in southern Africa, as evidenced by thickening of the MTZ by 10-20 km (Blum & Shen, 2004; Boyce & Cottaar, 2021). This would raise the depth of the Co-St and OEN-HCEN transitions to $\sim$250 km depth (Schmerr, 2015). While cool mantle temperatures are not observed beneath all cratons (e.g., Thompson et al., 2011), for the thicker cratons, this may inhibit phase transitions associated with the X, preventing its observation (Figure S6). Additionally, in some locations, ponding of chemical heterogeneity may not be possible at the margins of the craton where complex flow is present due to edge-driven convection (King & Anderson, 1998; Currie & van Wijk, 2016).

5 Conclusions

X discontinuity structure beneath the African continent and surrounding ocean islands is vastly extended using widespread recordings of Pds RFs. The X is observed beneath the EARS, Morocco, Cameroon, Hoggar and several ocean islands (Canaries, Cape Verde, Madagascar, Réunion and Mauritius) at 233–340 km depth using a normalized vote mapping approach.

The X is recorded across a broad range of depths and amplitudes. With no apparent relationship to upper mantle temperature and widespread occurrence across variable geodynamic settings, a multigenetic origin of the X is required below continents. Observations of the X are typically collocated with surface regions of Cenozoic magmatism and Quaternary volcanoes, suggesting that surface magmatism is intrinsically linked to upper mantle chemical heterogeneity, however some notable exceptions exist. The broad connection may be explained by the presence of plumes of variable thermochemical nature beneath parts/all of the EARS, the Canaries/Morocco, Cape Verde, southern Madagascar and Réunion. However, it is difficult to explain the cause of upper mantle chemical heterogeneity beneath Cameroon, Hoggar and central Madagascar by a plume related mechanism where upper mantle processes are mostly likely responsible for surface magmatism. Whilst null observations dominate beneath cratons, it remains uncertain if this is linked to localized geodynamic conditions (e.g., lack of chemical heterogeneity or thermal anomaly) or is an artifact due to masking by shallower structure.

Acknowledgments

This project received funding from the Natural Environment Research Council (grant number NE/L002507/1) awarded to S. Pugh, and the European Research Council (ERC) under the European Union's Horizon 2020 research and innovation program (grant agreement No. 804071-ZoomDeep) awarded to S. Cottaar. C. J. Ebinger acknowledges NSFGEO-NERC award 1824417. I. Bastow acknowledges support from Natural Environment Research Council grant number NE/S014136/1.

Open Research

The facilities of IRIS Data Services, and specifically the IRIS Data Management Center, alongside the AUSPASS, GEOFON, ORFEUS and RESIF data centres, were used for access to waveforms, related metadata, and/or derived products used in this study. IRIS Data Services are funded through the Seismological Facilities for the Advancement of Geoscience (SAGE) Award of the National Science Foundation under Cooperative Support Agreement EAR-1851048. The waveform data used in this study are from the following networks: 1C (Velasco et al., 2011), 2H (Keir & Hammond, 2009), 2L (Lange & Soler, 2019), 3D (Thomas, 2010), 4H (Hammond et al., 2011), 5H (Hammond, 2011), 6A (Heit, Yuan, Jokat, et al., 2010), 6H (Helffrich & Fonseca, 2011), 6R (I. D. Bastow, 2019), 7C (Vergne et al., 2014), 8A (Nyblade, 2015a), 9A (Weber et al., 2007), 9C (Heit, Yuan, & Mancilla, 2010), AF (Penn State University, 2004), G (Institut de physique du globe de Paris (IPGP) & École et Observatoire des Sciences de la Terre de Strasbourg (EOST), 1982), GE (GEOFON Data Centre, 1993), GH (Ghana Geological Survey, 2012), GT (Albuquerque Seismological Laboratory (ASL)/USGS, 1993), IB (Institute Earth Sciences "Jaume Almera" CSIC (ICTJA Spain), 2007), II (Scripps Institution of Oceanography, 1986), IU (Albuquerque Seismological Laboratory (ASL)/USGS, 1988), IV (INGV Seismological Data Centre, 1997), MN (MedNet Project Partner Institutions, 1988), NJ (Centre for Geodesy and Geodynamics, 2009), NR (Utrecht University (UU Netherlands), 1983), PF (Observatoire Volcanologique Du Piton De La Fournaise (OVPF) & Institut De Physique Du Globe De Paris (IPGP), 2008), PM (Instituto Português do Mar e da Atmosfera, I.P., 2006), TZ (Aubreya Adams, 2017), WM (San Fernando Royal Naval Observatory (ROA) et al., 1996), XA (Silver, 1997), XB (Wiens & Nyblade, 2005), XB (Levander et al., 2009), XC (Kind, 1998), XD (Owens & Nyblade, 1994), XI (Nyblade, 2000), XJ (Ebinger, 2013), XK (Gao et al., 2012), XM (The ARGOS Project, 2012), XV (Wysession et al., 2011), XW (Leroy et al., 2009), XW (Nyblade, 2017), Y1 (Ebinger, 2018), YA (Ebinger, 2012), YF (van der Lee et al., 1999), YH (Nyblade, 2010), YI (Gaherty & Shillington, 2010), YQ (Gaherty et al., 2013), YQ (Keir et al., 2017), YR (Levèque & RESIF, 2010), YV (Barruol et al., 2017), YY (Keranen, 2013), ZE (Ebinger, 2007), ZE (Tilmann et al., 2012), ZF (Fontaine et al., 2015), ZI (Wookey et al., 2011), ZK (Gao, 2009), ZP (Nyblade, 2007), ZS (Deschamps et al., 2007), ZT (Nyblade, 2015b) and ZV (Ebinger, 2014). Networks 1B, BX, TT, XJ, XJ, XM, YF, YJ, YK, YW, YZ, ZC, ZF, ZP, ZQ and ZU do not have DOIs and are detailed in Table S1. This study uses ObsPy (Megies et al., 2011). Scripts for receiver function creation and processing are available through SMURFPy (Cottaar et al., 2020).

References

Adams, A., & Nyblade, A. A. (2011). Shear wave velocity structure of the southern African upper mantle with implications for the uplift of southern Africa. *Geophys. J. Int.*, *186*(2), 808–824. Retrieved from `https://doi.org/10.1111/j.1365-246x.2011.05072.x` doi: 10.1111/j.1365-246x.2011.05072.x

Akaogi, M., Oohata, M., Kojitani, H., & Kawaji, H. (2011). Thermodynamic properties of stishovite by low-temperature heat capacity measurements and the coesite-stishovite transition boundary. *Am. Mineral.*, *96*(8-9), 1325–1330. Retrieved from `https://doi.org/10.2138/am.2011.3748` doi: 10.2138/am.2011.3748

Albuquerque Seismological Laboratory (ASL)/USGS. (1988). *Global Seismograph Network - IRIS/USGS.* International Federation of Digital Seismograph Networks. Retrieved from `https://www.fdsn.org/networks/detail/IU/` doi: 10.7914/SN/IU

Albuquerque Seismological Laboratory (ASL)/USGS. (1993). *Global Telemetered Seismograph Network (USAF/USGS).* International Federation of Digital Seismograph Networks. Retrieved from `https://www.fdsn.org/networks/detail/GT/` doi: 10.7914/SN/GT

Aubreya Adams. (2017). *Ol Doinyo Lengai, TZ Volcano Monitoring.* International Federation of Digital Seismograph Networks. Retrieved from `https://www.fdsn.org/networks/detail/TZ/` doi: 10.7914/SN/TZ

Ballmer, M. D., Ito, G., Wolfe, C. J., & Solomon, S. C. (2013). Double layering of a thermochemical plume in the upper mantle beneath Hawaii. *Earth Planet. Sci. Lett.*, *376*, 155–164. Retrieved from `https://doi.org/10.1016/j.epsl.2013.06.022` doi: 10.1016/j.epsl.2013.06.022

Barfod, D. N., Ballentine, C. J., Halliday, A. N., & Fitton, J. G. (1999). Noble gases in the cameroon line and the he, ne, and ar isotopic compositions of high μ (HIMU) mantle. *J. Geophys. Res. Solid Earth*, *104*(B12), 29509–29527. Retrieved from `https://doi.org/10.1029/1999jb900280` doi: 10.1029/1999jb900280

Barruol, G., Sigloch, K., RHUM-RUM Group, & RESIF. (2017). *RHUM-RUM experiment, 2011-2015, code YV (Réunion Hotspot and Upper Mantle – Réunion's Unterer Mantel) funded by ANR, DFG, CNRS-INSU, IPEV, TAAF, instrumented by DEPAS, INSU-OBS, AWI and the Universities of Muenster, Bonn, La Réunion.* RESIF - Réseau Sismologique et géodésique Français. Retrieved from `https://seismology.resif.fr/networks/#/YV__2011` doi: 10.15778/RESIF.YV2011

Bastow, I., Nyblade, A., Stuart, G., Rooney, T., & Benoit, M. (2008). Upper Mantle Seismic Structure Beneath the Ethiopian Hotspot: Rifting at the Edge of the African Low Velocity Anomaly. *Geochem. Geophys. Geosyst.*, *9*(12). doi: 10.1029/2008GC002107

Bastow, I. D. (2019). *Turkana rift arrays to investigate lithospheric strains - uk component.* International Federation of Digital Seismograph Networks. Retrieved from https://www.fdsn.org/networks/detail/6R_2019/ doi: 10.7914/SN/6R_2019

Begg, G., Griffin, W., Natapov, L., O'Reilly, S. Y., Grand, S., O'Neill, C., ... Bowden, P. (2009). The lithospheric architecture of Africa: Seismic tomography, mantle petrology, and tectonic evolution. *Geosphere*, *5*(1), 23-50. Retrieved from https://doi.org/10.1130/GES00179.1 doi: 10.1130/GES00179.1

Berthod, C., Bachèlery, P., Jorry, S., Pitel-Roudaut, M., Ruffet, G., Revillon, S., ... Doucelance, R. (2022). First characterization of the volcanism in the southern Mozambique Channel: Geomorphological and structural analyses. *Mar. Geol.*, *445*, 106755. Retrieved from https://doi.org/10.1016/j.margeo.2022.106755 doi: 10.1016/j.margeo.2022.106755

Bezada, M. J., Humphreys, E. D., Davila, J., Carbonell, R., Harnafi, M., Palomeras, I., & Levander, A. (2014). Piecewise delamination of Moroccan lithosphere from beneath the Atlas Mountains. *Geochem. Geophys. Geosyst.*, *15*(4), 975–985. Retrieved from https://doi.org/10.1002/2013gc005059 doi: 10.1002/2013gc005059

Bina, C. R., & Helffrich, G. (1994). Phase transition Clapeyron slopes and transition zone seismic discontinuity topography. *J. Geophys. Res. Solid Earth*, *99*(B8), 15853. Retrieved from https://doi.org/10.1029/94jb00462 doi: 10.1029/94jb00462

Blum, J., & Shen, Y. (2004). Thermal, hydrous, and mechanical states of the mantle transition zone beneath southern Africa. *Earth Planet. Sci. Lett.*, *217*(3-4), 367–378. Retrieved from https://doi.org/10.1016/s0012-821x(03)00628-9 doi: 10.1016/s0012-821x(03)00628-9

Boyce, A., Bastow, I. D., Cottaar, S., Kounoudis, R., Courbeville, J. G. D., Caunt, E., & Desai, S. (2021). AFRP20: New P-wavespeed model for the African mantle reveals two whole-mantle plumes below East Africa and Neoproterozoic modification of the Tanzania craton. *Geochem. Geophys. Geosyst.*, *22*(3). Retrieved from https://doi.org/10.1029/2020gc009302 doi: 10.1029/2020gc009302

Boyce, A., & Cottaar, S. (2021). Insights into deep mantle thermochemical contributions to African magmatism from converted seismic phases. *Geochem. Geophys. Geosyst.*, *22*(3). Retrieved from https://doi.org/10.1029/

2020gc009478 doi: 10.1029/2020gc009478

Buchen, J., Marquardt, H., Speziale, S., Kawazoe, T., Ballaran, T. B., & Kurnosov, A. (2018). High-pressure single-crystal elasticity of wadsleyite and the seismic signature of water in the shallow transition zone. *Earth Planet. Sci. Lett.*, *498*, 77–87. Retrieved from https://doi.org/10.1016/j.epsl.2018.06.027 doi: 10.1016/j.epsl.2018.06.027

Celli, N. L., Lebedev, S., Schaeffer, A. J., & Gaina, C. (2020). African cratonic lithosphere carved by mantle plumes. *Nat. Commun.*, *11*(1). Retrieved from https://doi.org/10.1038/s41467-019-13871-2 doi: 10.1038/s41467-019-13871-2

Celli, N. L., Lebedev, S., Schaeffer, A. J., Ravenna, M., & Gaina, C. (2020). The upper mantle beneath the South Atlantic Ocean, South America and Africa from waveform tomography with massive data sets. *Geophys. J. Int.*, *221*(1), 178–204. Retrieved from https://doi.org/10.1093/gji/ggz574 doi: 10.1093/gji/ggz574

Centre for Geodesy and Geodynamics. (2009). *Nigerian National Network of Seismographic Stations (NNNSS).* International Federation of Digital Seismograph Networks. Retrieved from https://www.fdsn.org/networks/detail/NJ/ doi: 10.7914/SN/NJ

Chang, S.-J., Ferreira, A. M., Ritsema, J., van Heijst, H. J., & Woodhouse, J. H. (2015). Joint inversion for global isotropic and radially anisotropic mantle structure including crustal thickness perturbations. *J. Geophys. Res. Solid Earth*, *120*(6), 4278–4300. Retrieved from https://doi.org/10.1002/2014JB011824 doi: 10.1002/2014JB011824

Chang, S.-J., Kendall, E., Davaille, A., & Ferreira, A. M. G. (2020). The evolution of mantle plumes in East Africa. *J. Geophys. Res. Solid Earth*, *125*(12). Retrieved from https://doi.org/10.1029/2020jb019929 doi: 10.1029/2020jb019929

Chorowicz, J. (2005). The East African rift system. *J. Afr. Earth Sci.*, *43*(1-3), 379–410. Retrieved from https://doi.org/10.1016/j.jafrearsci.2005.07.019 doi: 10.1016/j.jafrearsci.2005.07.019

Civiero, C., Goes, S., Hammond, J. O., Fishwick, S., Ahmed, A., Ayele, A., . . . others (2016). Small-scale thermal upwellings under the northern East African

Rift from S travel time tomography. *J. Geophys. Res. Solid Earth*, *121*(10), 7395–7408. Retrieved from https://doi.org/10.1002/2016JB013070 doi: 10.1002/2016JB013070

Civiero, C., Hammond, J. O., Goes, S., Fishwick, S., Ahmed, A., Ayele, A., ... others (2015). Multiple mantle upwellings in the transition zone beneath the northern East-African Rift system from relative P-wave travel-time tomography. *Geochem. Geophys. Geosyst.*, *16*(9), 2949–2968. Retrieved from https://doi.org/10.1002/2015GC005948 doi: 10.1002/2015GC005948

Civiero, C., Strak, V., Custódio, S., Silveira, G., Rawlinson, N., Arroucau, P., & Corela, C. (2018). A common deep source for upper-mantle upwellings below the Ibero-western Maghreb region from teleseismic P-wave travel-time tomography. *Earth Planet. Sci. Lett.*, *499*, 157–172. Retrieved from https://doi.org/10.1016/j.epsl.2018.07.024 doi: 10.1016/j.epsl.2018.07.024

Cottaar, S., & Deuss, A. (2016). Large-scale mantle discontinuity topography beneath Europe: Signature of akimotoite in subducting slabs. *J. Geophys. Res. Solid Earth*, *121*(1), 279–292. Retrieved from https://doi.org/10.1002/2015jb012452 doi: 10.1002/2015jb012452

Cottaar, S., Pugh, S., Boyce, A., & Jenkins, J. (2020). *sannecottaar/smurfpy: SMURFPy.* Zenodo. Retrieved from https://zenodo.org/record/4337258 doi: 10.5281/ZENODO.4337258

Courgeon, S., Jorry, S., Camoin, G., BouDagher-Fadel, M., Jouet, G., Révillon, S., ... Droxler, A. (2016). Growth and demise of Cenozoic isolated carbonate platforms: New insights from the Mozambique Channel seamounts (SW Indian Ocean). *Mar. Geol.*, *380*, 90–105. Retrieved from https://doi.org/10.1016/j.margeo.2016.07.006 doi: 10.1016/j.margeo.2016.07.006

Courgeon, S., Jorry, S., Jouet, G., Camoin, G., BouDagher-Fadel, M., Bachèlery, P., ... Guérin, C. (2017). Impact of tectonic and volcanism on the Neogene evolution of isolated carbonate platforms (SW Indian Ocean). *Sediment. Geol.*, *355*, 114–131. Retrieved from https://doi.org/10.1016/j.sedgeo.2017.04.008 doi: 10.1016/j.sedgeo.2017.04.008

Courtillot, V., Davaille, A., Besse, J., & Stock, J. (2003). Three distinct types of hotspots in the Earth's mantle. *Earth Planet. Sci. Lett.*, *205*(3-4), 295–308. Retrieved from https://doi.org/10.1016/s0012-821x(02)01048-8 doi:

10.1016/s0012-821x(02)01048-8

Crotwell, H. P., Owens, T. J., & Ritsema, J. (1999). The TauP toolkit: Flexible seismic travel-time and ray-path utilities. *Seis. Res. Lett.*, *70*(2), 154–160. Retrieved from https://doi.org/10.1785/gssrl.70.2.154 doi: 10.1785/gssrl.70.2.154

Cucciniello, C., Melluso, L., le Roex, A. P., Jourdan, F., Morra, V., de' Gennaro, R., & Grifa, C. (2017). From olivine nephelinite, basanite and basalt to peralkaline trachyphonolite and comendite in the Ankaratra volcanic complex, Madagascar: 40 Ar/ 39 Ar ages, phase compositions and bulk-rock geochemical and isotopic evolution. *Lithos*, *274-275*, 363–382. Retrieved from https://doi.org/10.1016/j.lithos.2016.12.026 doi: 10.1016/j.lithos.2016.12.026

Currie, C. A., & van Wijk, J. (2016). How craton margins are preserved: Insights from geodynamic models. *J. Geodyn.*, *100*, 144–158. Retrieved from https://doi.org/10.1016/j.jog.2016.03.015 doi: 10.1016/j.jog.2016.03.015

Daly, M. C., Green, P., Watts, A. B., Davies, O., Chibesakunda, F., & Walker, R. (2020). Tectonics and landscape of the Central African Plateau and their implications for a propagating Southwestern Rift in Africa. *Geochem. Geophys. Geosyst.*, *21*(6). Retrieved from https://doi.org/10.1029/2019gc008746 doi: 10.1029/2019gc008746

Dannberg, J., & Sobolev, S. V. (2015). Low-buoyancy thermochemical plumes resolve controversy of classical mantle plume concept. *Nat. Commun.*, *6*(1). Retrieved from https://doi.org/10.1038/ncomms7960 doi: 10.1038/ncomms7960

Dasgupta, R., Mallik, A., Tsuno, K., Withers, A. C., Hirth, G., & Hirschmann, M. M. (2013). Carbon-dioxide-rich silicate melt in the Earth's upper mantle. *Nature*, *493*(7431), 211–215. Retrieved from https://doi.org/10.1038/nature11731 doi: 10.1038/nature11731

Davaille, A., Stutzmann, E., Silveira, G., Besse, J., & Courtillot, V. (2005). Convective patterns under the Indo-Atlantic ≪ box ≫. *Earth Planet. Sci. Lett.*, *239*(3-4), 233–252. Retrieved from https://doi.org/10.1016/j.epsl.2005.07.024 doi: 10.1016/j.epsl.2005.07.024

De Plaen, R. S. M., Bastow, I. D., Chambers, E. L., Keir, D., Gallacher, R. J., &

Keane, J. (2014). The development of magmatism along the Cameroon Volcanic Line: Evidence from seismicity and seismic anisotropy. *J. Geophys. Res. Solid Earth*, *119*(5), 4233–4252. Retrieved from https://doi.org/10.1002/2013jb010583 doi: 10.1002/2013jb010583

Debayle, E., Dubuffet, F., & Durand, S. (2016). An automatically updated s-wave model of the upper mantle and the depth extent of azimuthal anisotropy. *Geophys. Res. Lett.*, *43*(2), 674–682.

de Gouveia, S. V., Besse, J., de Lamotte, D. F., Greff-Lefftz, M., Lescanne, M., Gueydan, F., & Leparmentier, F. (2018). Evidence of hotspot paths below Arabia and the Horn of Africa and consequences on the Red Sea opening. *Earth Planet. Sci. Lett.*, *487*, 210–220. Retrieved from https://doi.org/10.1016/j.epsl.2018.01.030 doi: 10.1016/j.epsl.2018.01.030

Deniel, C. (1998). Geochemical and isotopic (Sr, Nd, Pb) evidence for plume-lithosphere interactions in the genesis of Grande Comore magmas (Indian Ocean). *Chem. Geol.*, *144*(3-4), 281–303. Retrieved from https://doi.org/10.1016/s0009-2541(97)00139-3 doi: 10.1016/s0009-2541(97)00139-3

Déruelle, B., Moreau, C., Nkoumbou, C., Kambou, R., Lissom, J., Njonfang, E., … Nono, A. (1991). The Cameroon Line: A review. In *Magmatism in extensional structural settings* (pp. 274–327). Springer Berlin Heidelberg. Retrieved from https://doi.org/10.1007/978-3-642-73966-8_12 doi: 10.1007/978-3-642-73966-8_12

Deschamps, A., Déverchère, J., & Ferdinand, R. (2007). *SEISMOTANZ'07.* RESIF - Réseau Sismologique et géodésique Français. Retrieved from https://seismology.resif.fr/networks/#/ZS__2007 doi: 10.15778/RESIF.ZS2007

Deuss, A., & Woodhouse, J. H. (2002). A systematic search for mantle discontinuities using ss-precursors. *Geophys. Res. Lett.*, *29*(8), 90–1. Retrieved from https://doi.org/10.1029/2002GL014768 doi: 10.1029/2002GL014768

Deuss, A., & Woodhouse, J. H. (2004). The nature of the Lehmann discontinuity from its seismological Clapeyron slopes. *Earth Planet. Sci. Lett.*, *225*(3-4), 295–304. Retrieved from https://doi.org/10.1016/j.epsl.2004.06.021 doi: 10.1016/j.epsl.2004.06.021

Doucelance, R., Escrig, S., Moreira, M., Gariépy, C., & Kurz, M. D. (2003). Pb-sr-he isotope and trace element geochemistry of the cape verde archipelago. *Geochim. Cosmochim. Acta.*, *67*(19), 3717–3733. Retrieved from https://doi.org/10.1016/s0016-7037(03)00161-3 doi: 10.1016/s0016-7037(03)00161-3

Dueker, K. G., & Sheehan, A. F. (1997). Mantle discontinuity structure from midpoint stacks of converted p to s waves across the yellowstone hotspot track. *J. Geophys. Res. Solid Earth*, *102*(B4), 8313–8327. Retrieved from https://doi.org/10.1029/96JB03857 doi: 10.1029/96JB03857

Dueker, K. G., & Sheehan, A. F. (1998). Mantle discontinuity structure beneath the colorado rocky mountains and high plains. *J. Geophys. Res. Solid Earth*, *103*(B4), 7153–7169. Retrieved from https://doi.org/10.1029/97jb03509 doi: 10.1029/97jb03509

Duggen, S., Hoernle, K., Hauff, F., Klügel, A., Bouabdellah, M., & Thirlwall, M. (2009). Flow of Canary mantle plume material through a subcontinental lithospheric corridor beneath Africa to the Mediterranean. *Geology*, *37*(3), 283–286. Retrieved from https://doi.org/10.1130/g25426a.1 doi: 10.1130/g25426a.1

Dziewonski, A. M., & Anderson, D. L. (1981). Preliminary reference Earth model. *Phys. Earth Planet. Int.*, *25*(4), 297–356. Retrieved from https://doi.org/10.1016/0031-9201(81)90046-7 doi: 10.1016/0031-9201(81)90046-7

Ebinger, C. J. (1989). Tectonic development of the western branch of the East African rift system. *Geol. Soc. Am.*, *101*(7), 885–903. Retrieved from https://doi.org/10.1130/0016-7606(1989)101<0885:TDOTWB>2.3.CO;2 doi: 10.1130/0016-7606(1989)101⟨0885:TDOTWB⟩2.3.CO;2

Ebinger, C. J. (2007). *AFAR07.* International Federation of Digital Seismograph Networks. Retrieved from https://www.fdsn.org/networks/detail/ZE_2007/ doi: 10.7914/SN/ZE_2007

Ebinger, C. J. (2012). *Dynamics of the Lake Kivu System.* International Federation of Digital Seismograph Networks. Retrieved from https://www.fdsn.org/networks/detail/YA_2012/ doi: 10.7914/SN/YA_2012

Ebinger, C. J. (2013). *Magadi-Natron magmatic rifting studies.* International Federation of Digital Seismograph Networks. Retrieved from https://www.fdsn.org/networks/detail/XJ_2013/ doi: 10.7914/SN/XJ_2013

Ebinger, C. J. (2014). *Southern Lake Tanganyika experiment.* International Federation of Digital Seismograph Networks. Retrieved from https://www.fdsn.org/networks/detail/ZV_2014/ doi: 10.7914/SN/ZV_2014

Ebinger, C. J. (2018). *Crust and mantle structure and the expression of extension in the Turkana depression of Kenya and Ethiopia.* International Federation of Digital Seismograph Networks. Retrieved from https://www.fdsn.org/networks/detail/Y1_2018/ doi: 10.7914/SN/Y1_2018

Ebinger, C. J., Keir, D., Bastow, I. D., Whaler, K., Hammond, J. O. S., Ayele, A., ... Hautot, S. (2017). Crustal structure of active deformation zones in Africa: Implications for global crustal processes. *Tectonics*, *36*(12), 3298–3332. Retrieved from https://doi.org/10.1002/2017tc004526 doi: 10.1002/2017tc004526

Ebinger, C. J., & Sleep, N. H. (1998). Cenozoic magmatism throughout east africa resulting from impact of a single plume. *Nature*, *395*(6704), 788–791. Retrieved from https://doi.org/10.1038/27417 doi: 10.1038/27417

Emerick, C., & Duncan, R. (1982). Age progressive volcanism in the Comores Archipelago, western Indian Ocean and implications for Somali plate tectonics. *Earth Planet. Sci. Lett.*, *60*(3), 415–428. Retrieved from https://doi.org/10.1016/0012-821x(82)90077-2 doi: 10.1016/0012-821x(82)90077-2

Emry, E. L., Shen, Y., Nyblade, A. A., Flinders, A., & Bao, X. (2019). Upper Mantle Earth Structure in Africa From Full-Wave Ambient Noise Tomography. *Geochem. Geophys. Geosyst.*, *20*(1), 120–147. Retrieved from https://doi.org/10.1029/2018gc007804 doi: 10.1029/2018gc007804

Fairhead, J., & Binks, R. (1991). Differential Opening of the Central and South Atlantic Oceans and the Opening of the West African Rift System. *Tectonophysics*, *187*(1-3), 191–203.

Fishwick, S. (2010). Surface wave tomography: Imaging of the lithosphere-asthenosphere boundary beneath central and southern Africa? *Lithos*, *120*(1-2), 63–73. Retrieved from https://doi.org/10.1016/j.lithos.2010.05.011 doi: 10.1016/j.lithos.2010.05.011

Fitton, J. (1980). The Benue trough and Cameroon Line — A migrating rift system in West Africa. *Earth Planet. Sci. Lett.*, *51*(1), 132–138. Retrieved from https://doi.org/10.1016/0012-821x(80)90261-7 doi: 10.1016/0012-821x(80)90261-7

Fontaine, F. R., Barruol, G., & Gonzalez, A. (2015). *Rivière des Pluies Project, La Réunion Island, 2015-2018.* RESIF - Réseau Sismologique et géodésique Français. Retrieved from https://seismology.resif.fr/networks/#/ZF__2015 doi: 10.15778/RESIF.ZF2015

Forte, A. M., Quéré, S., Moucha, R., Simmons, N. A., Grand, S. P., Mitrovica, J. X., & Rowley, D. B. (2010). Joint seismic-geodynamic-mineral physical modelling of African geodynamics: A reconciliation of deep-mantle convection with surface geophysical constraints. *Earth Planet. Sci. Lett.*, *295*(3-4), 329–341. Retrieved from https://doi.org/10.1016/j.epsl.2010.03.017 doi: 10.1016/j.epsl.2010.03.017

French, S. W., & Romanowicz, B. (2015). Broad plumes rooted at the base of the Earth's mantle beneath major hotspots. *Nature*, *525*(7567), 95–99. Retrieved from https://doi.org/10.1038/nature14876 doi: 10.1038/nature14876

French, S. W., & Romanowicz, B. A. (2014). Whole-mantle radially anisotropic shear velocity structure from spectral-element waveform tomography. *Geophys. J. Int.*, *199*(3), 1303–1327. Retrieved from https://doi.org/10.1093/gji/ggu334 doi: 10.1093/gji/ggu334

Fullea, J., Lebedev, S., Martinec, Z., & Celli, N. L. (2021). WINTERC-g: mapping the upper mantle thermochemical heterogeneity from coupled geophysical-petrological inversion of seismic waveforms, heat flow, surface elevation and gravity satellite data. *Geophys. J. Int.*, *226*(1), 146–191. Retrieved from https://doi.org/10.1093/gji/ggab094 doi: 10.1093/gji/ggab094

Furman, T., Bryce, J., Rooney, T., Hanan, B., Yirgu, G., & Ayalew, D. (2006). Heads and tails: 30 million years of the Afar plume. *Geological Society, London, Special Publications*, *259*(1), 95–119. Retrieved from https://doi.org/10.1144/gsl.sp.2006.259.01.09 doi: 10.1144/gsl.sp.2006.259.01.09

Gaherty, J., Ebinger, C. J., Nyblade, A. A., & Shillington, D. (2013). *Study of extension and magmatism in Malawi and Tanzania.* International Federation of Digital Seismograph Networks. Retrieved from https://www.fdsn.org/networks/detail/YQ_2013/ doi: 10.7914/SN/YQ_2013

Gaherty, J., & Shillington, D. (2010). *2009 Malawi Earthquake RAMP Response.* International Federation of Digital Seismograph Networks. Retrieved from https://www.fdsn.org/networks/detail/YI_2010/ doi:

10.7914/SN/YI_2010

Gallacher, R., & Bastow, I. (2012). The Development of Magmatism Along the Cameroon Volcanic Line: Evidence from Teleseismic Receiver Functions. *Tectonics*, *31*. doi: 10.1029/2011TC003028

Gao, S. (2009). *Afar depression dense seismic array.* International Federation of Digital Seismograph Networks. Retrieved from https://www.fdsn.org/networks/detail/ZK_2009/ doi: 10.7914/SN/ZK_2009

Gao, S., Liu, K., Abdelsalam, M., & Hogan, J. (2012). *Seismic arrays for African Rift initation.* International Federation of Digital Seismograph Networks. Retrieved from https://www.fdsn.org/networks/detail/XK_2012/ doi: 10.7914/SN/XK_2012

Geldmacher, J., & Hoernle, K. (2000). The 72 Ma geochemical evolution of the Madeira hotspot (eastern North Atlantic): recycling of Paleozoic (≤500 Ma) oceanic lithosphere. *Earth Planet. Sci. Lett.*, *183*(1-2), 73–92. Retrieved from https://doi.org/10.1016/s0012-821x(00)00266-1 doi: 10.1016/s0012-821x(00)00266-1

GEOFON Data Centre. (1993). *GEOFON Seismic Network.* Deutsches GeoForschungsZentrum GFZ. Retrieved from http://geofon.gfz-potsdam.de/doi/network/GE doi: 10.14470/TR560404

Ghana Geological Survey. (2012). *Ghana digital seismic network.* International Federation of Digital Seismograph Networks. Retrieved from https://www.fdsn.org/networks/detail/GH/ doi: 10.7914/SN/GH

Graham, D., Lupton, J., Albarède, F., & Condomines, M. (1990). Extreme temporal homogeneity of helium isotopes at piton de la fournaise, réunion island. *Nature*, *347*(6293), 545–548. Retrieved from https://doi.org/10.1038/347545a0 doi: 10.1038/347545a0

Gurenko, A. A., Hoernle, K. A., Hauff, F., Schmincke, H.-U., Han, D., Miura, Y. N., & Kaneoka, I. (2006). Major, trace element and Nd-Sr-Pb-O-He-Ar isotope signatures of shield stage lavas from the central and western Canary Islands: Insights into mantle and crustal processes. *Chem. Geol.*, *233*(1-2), 75–112. Retrieved from https://doi.org/10.1016/j.chemgeo.2006.02.016 doi: 10.1016/j.chemgeo.2006.02.016

Gurenko, A. A., Sobolev, A. V., Hoernle, K. A., Hauff, F., & Schmincke, H.-U.

(2009). Enriched, HIMU-type peridotite and depleted recycled pyroxenite in the Canary plume: A mixed-up mantle. *Earth Planet. Sci. Lett.*, *277*(3-4), 514–524. Retrieved from https://doi.org/10.1016/j.epsl.2008.11.013 doi: 10.1016/j.epsl.2008.11.013

Hammond, J. (2011). *Eritrea seismic project.* International Federation of Digital Seismograph Networks. Retrieved from https://www.fdsn.org/networks/detail/5H_2011/ doi: 10.7914/SN/5H_2011

Hammond, J., Goitom, B., Kendall, J. M., & Ogubazghi, G. (2011). *Nabro urgency array.* International Federation of Digital Seismograph Networks. Retrieved from https://www.fdsn.org/networks/detail/4H_2011/ doi: 10.7914/SN/4H_2011

Hansen, S. E., Nyblade, A. A., & Benoit, M. H. (2012). Mantle structure beneath Africa and Arabia from adaptively parameterized P-wave tomography: Implications for the origin of Cenozoic Afro-Arabian tectonism. *Earth Planet. Sci. Lett.*, *319*, 23–34. doi: 10.1016/j.epsl.2011.12.023

Heit, B., Yuan, X., Jokat, W., Weber, M., & Geissler, W. (2010). *WALPASS Network, Namibia, 2010/2012.* Deutsches GeoForschungsZentrum GFZ. Retrieved from http://geofon.gfz-potsdam.de/doi/network/6A/2010 doi: 10.14470/1N134371

Heit, B., Yuan, X., & Mancilla, F. D. L. (2010). *High resolution seismological profiling across Sierra Nevada (HIRE).* Deutsches GeoForschungsZentrum GFZ. Retrieved from http://geofon.gfz-potsdam.de/doi/network/9C/2010 doi: 10.14470/4P7565788335

Helffrich, G. (2000). Topography of the transition zone seismic discontinuities. *Rev. Geophys.*, *38*(1), 141–158. Retrieved from https://doi.org/10.1029/1999rg000060 doi: 10.1029/1999rg000060

Helffrich, G. (2002). Thermal variations in the mantle inferred from 660 km discontinuity topography and tomographic wave speed variations. *Geophys. J. Int.*, *151*(3), 935–943. Retrieved from https://doi.org/10.1046/j.1365-246x.2002.01824.x doi: 10.1046/j.1365-246x.2002.01824.x

Helffrich, G., & Fonseca, J. F. B. D. (2011). *Mozambique rift tomography.* International Federation of Digital Seismograph Networks. Retrieved from https://www.fdsn.org/networks/detail/6H_2011/ doi: 10.7914/SN/6H_2011

Ho, T., Priestley, K., & Debayle, E. (2016). A global horizontal shear velocity model of the upper mantle from multimode love wave measurements. *Geophys. J. Int.*, *207*(1), 542–561. Retrieved from https://doi.org/10.1093/gji/ggw292 doi: 10.1093/gji/ggw292

Hoggard, M. J., Czarnota, K., Richards, F. D., Huston, D. L., Jaques, A. L., & Ghelichkhan, S. (2020). Global distribution of sediment-hosted metals controlled by craton edge stability. *Nat. Geosci.*, *13*(7), 504–510. Retrieved from https://doi.org/10.1038/s41561-020-0593-2 doi: 10.1038/s41561-020-0593-2

INGV Seismological Data Centre. (1997). *Rete Sismica Nazionale (RSN).* Istituto Nazionale di Geofisica e Vulcanologia (INGV), Italy. Retrieved from http://cnt.rm.ingv.it/instruments/network/IV doi: 10.13127/SD/X0FXNH7QFY

Institut de physique du globe de Paris (IPGP), & École et Observatoire des Sciences de la Terre de Strasbourg (EOST). (1982). *GEOSCOPE, French Global Network of broad band seismic stations.* Institut de physique du globe de Paris (IPGP), Université de Paris. Retrieved from http://geoscope.ipgp.fr/networks/detail/G/ doi: 10.18715/GEOSCOPE.G

Institute Earth Sciences "Jaume Almera" CSIC (ICTJA Spain). (2007). *IberArray.* International Federation of Digital Seismograph Networks. Retrieved from https://www.fdsn.org/networks/detail/IB/ doi: 10.7914/SN/IB

Instituto Português do Mar e da Atmosfera, I.P. (2006). *Portuguese National Seismic Network.* International Federation of Digital Seismograph Networks. Retrieved from https://www.fdsn.org/networks/detail/PM/ doi: 10.7914/SN/PM

Jackson, M. G., Becker, T., & Konter, J. (2018). Evidence for a deep mantle source for EM and HIMU domains from integrated geochemical and geophysical constraints. *Earth Planet. Sci. Lett.*, *484*, 154–167. Retrieved from https://doi.org/10.1016/j.epsl.2017.11.052 doi: 10.1016/j.epsl.2017.11.052

Jackson, M. G., Konter, J. G., & Becker, T. (2017). Primordial helium entrained by the hottest mantle plumes. *Nature*, *542*(7641), 340–343. Retrieved from https://doi.org/10.1038/nature21023 doi: 10.1038/nature21023

Jenkins, J., Cottaar, S., White, R., & Deuss, A. (2016). Depressed mantle discontinuities beneath Iceland: Evidence of a garnet controlled 660 km discontinuity? *Earth Planet. Sci. Lett.*, *433*, 159–168. Retrieved from https://doi.org/10.1016/j.epsl.2015.10.053 doi: 10.1016/j.epsl.2015.10.053

Jones, D. (2020). *East african rift temperature and heat flow model (earth).* British Geological Survey. Retrieved from https://www.bgs.ac.uk/services/ngdc/citedData/catalogue/e1bc2841-81c2-4b6e-ae5b-301f3bf82b68.html doi: 10.5285/E1BC2841-81C2-4B6E-AE5B-301F3BF82B68

Kaislaniemi, L., & van Hunen, J. (2014). Dynamics of lithospheric thinning and mantle melting by edge-driven convection: Application to Moroccan Atlas mountains. *Geochem. Geophys. Geosyst.*, *15*(8), 3175–3189. Retrieved from https://doi.org/10.1002/2014gc005414 doi: 10.1002/2014gc005414

Katsura, T., & Ito, E. (1989). The system Mg_2SiO_4-Fe_2SiO_4 at high pressures and temperatures: Precise determination of stabilities of olivine, modified spinel, and spinel. *J. Geophys. Res. Solid Earth*, *94*(B11), 15663–15670. Retrieved from https://doi.org/10.1029/jb094ib11p15663 doi: 10.1029/jb094ib11p15663

Keir, D., Doubre, C., & Leroy, S. (2017). *Afar margin northern profile.* International Federation of Digital Seismograph Networks. Retrieved from https://www.fdsn.org/networks/detail/YQ_2017/ doi: 10.7914/SN/YQ_2017

Keir, D., & Hammond, J. O. (2009). *Afar0911.* International Federation of Digital Seismograph Networks. Retrieved from https://www.fdsn.org/networks/detail/2H_2009/ doi: 10.7914/SN/2H_2009

Kemp, M., Jenkins, J., Maclennan, J., & Cottaar, S. (2019). X-discontinuity and transition zone structure beneath Hawaii suggests a heterogeneous plume. *Earth Planet. Sci. Lett.*, *527*, 115781. Retrieved from https://doi.org/10.1016/j.epsl.2019.115781 doi: 10.1016/j.epsl.2019.115781

Keranen, K. (2013). *Exploring extensional tectonics beyond the Ethiopian Rift.* International Federation of Digital Seismograph Networks. Retrieved from https://www.fdsn.org/networks/detail/YY_2013/ doi: 10.7914/SN/YY_2013

Kind, R. (1998). *Namibia.* GFZ Data Services. Retrieved from https://geofon.gfz-potsdam.de/doi/network/XC/1998 doi: 10.14470/KP6443475642

King, S. D., & Anderson, D. L. (1998). Edge-driven convection. *Earth Planet.*

Sci. Lett., *160*(3-4), 289–296. Retrieved from https://doi.org/10.1016/s0012-821x(98)00089-2 doi: 10.1016/s0012-821x(98)00089-2

King, S. D., & Ritsema, J. (2000). African hot spot volcanism: Small-scale convection in the upper mantle beneath cratons. *Science*, *290*(5494), 1137–1140. Retrieved from https://doi.org/10.1126/science.290.5494.1137 doi: 10.1126/science.290.5494.1137

Kounoudis, R., Bastow, I. D., Ebinger, C. J., Ogden, C. S., Ayele, A., Bendick, R., … Kibret, B. (2021). Body-Wave Tomographic Imaging of the Turkana Depression: Implications for Rift Development and Plume-Lithosphere Interactions. *Geochem. Geophys. Geosyst.*, *22*(8). doi: 10.1029/2021gc009782

Lange, D., & Soler, V. (2019). *Monitoring the unrest of elhierro island with seismic observations.* GFZ Data Services. Retrieved from https://geofon.gfz-potsdam.de/doi/network/2L/2015 doi: 10.14470/7Y7560573304

Langston, C. A. (1979). Structure under Mount Rainier, Washington, inferred from teleseismic body waves. *J. Geophys. Res. Solid Earth*, *84*(B9), 4749. Retrieved from https://doi.org/10.1029/jb084ib09p04749 doi: 10.1029/jb084ib09p04749

Lee, D.-C., Halliday, A. N., Fitton, J., & Poli, G. (1994). Isotopic variations with distance and time in the volcanic islands of the Cameroon line: evidence for a mantle plume origin. *Earth Planet. Sci. Lett.*, *123*(1-3), 119–138. Retrieved from https://doi.org/10.1016/0012-821x(94)90262-3 doi: 10.1016/0012-821x(94)90262-3

Lekic, V., Cottaar, S., Dziewonski, A., & Romanowicz, B. (2012). Cluster analysis of global lower mantle tomography: A new class of structure and implications for chemical heterogeneity. *Earth Planet. Sci. Lett.*, *357*, 68–77. Retrieved from https://doi.org/10.1016/j.epsl.2012.09.014 doi: 10.1016/j.epsl.2012.09.014

Leroy, S., Keir, D., & Stuart, G. (2009). *Young conjugate margins lab in the Gulf of Aden.* International Federation of Digital Seismograph Networks. Retrieved from https://www.fdsn.org/networks/detail/XW_2009/ doi: 10.7914/SN/XW_2009

Levander, A., Humphreys, G., & Ryan, P. (2009). *Program to investigate convective Alboran Sea system overturn.* International Federation of Digital Seismograph Networks. Retrieved from https://www.fdsn.org/networks/detail/XB_2009/ doi: 10.7914/SN/XB_2009

Levèque, J.-J., & RESIF. (2010). *Horn of Africa (Ethiopa, Yemen) broad-band experiment (Horn of Africa, RESIF-SISMOB).* RESIF - Réseau Sismologique et géodésique Français. Retrieved from https://seismology.resif.fr/networks/#/YR__1999 doi: 10.15778/RESIF.YR1999

Liégeois, J.-P., Benhallou, A., Azzouni-Sekkal, A., Yahiaoui, R., & Bonin, B. (2005). The Hoggar swell and volcanism: Reactivation of the Precambrian Tuareg shield during Alpine convergence and West African Cenozoic volcanism. In *Plates, plumes and paradigms.* Geological Society of America. Retrieved from https://doi.org/10.1130/0-8137-2388-4.379 doi: 10.1130/0-8137-2388-4.379

Ligorria, J. P., & Ammon, C. J. (1999). Iterative deconvolution and receiver-function estimation. *Bull. Seis. Soc. Am.*, *89*(5), 1395–1400. Retrieved from https://doi.org/10.1785/BSSA0890051395 doi: 10.1785/BSSA0890051395

Lithgow-Bertelloni, C., & Silver, P. G. (1998). Dynamic topography, plate driving forces and the African superswell. *Nature*, *395*(6699), 269–272. Retrieved from https://doi.org/10.1038/26212 doi: 10.1038/26212

Lustrino, M., & Wilson, M. (2007). The circum-Mediterranean anorogenic Cenozoic igneous province. *Earth Sci. Rev.*, *81*(1-2), 1–65. Retrieved from https://doi.org/10.1016/j.earscirev.2006.09.002 doi: 10.1016/j.earscirev.2006.09.002

Marignier, A., Ferreira, A. M. G., & Kitching, T. (2020). The probability of mantle plumes in global tomographic models. *Geochem. Geophys. Geosyst.*, *21*(9). Retrieved from https://doi.org/10.1029/2020gc009276 doi: 10.1029/2020gc009276

Matthews, S., Shorttle, O., & Maclennan, J. (2016). The temperature of the icelandic mantle from olivine-spinel aluminum exchange thermometry. *Geochem. Geophys. Geosyst.*, *17*(11), 4725–4752. Retrieved from https://doi.org/10.1002/2016gc006497 doi: 10.1002/2016gc006497

MedNet Project Partner Institutions. (1988). *Mediterranean Very Broadband Seismographic Network (MedNet).* Istituto Nazionale di Geofisica e Vulcanologia (INGV). Retrieved from http://cnt.rm.ingv.it/instruments/network/MN doi: 10.13127/SD/FBBBTDTD6Q

Megies, T., Beyreuther, M., Barsch, R., Krischer, L., & Wassermann, J. (2011). ObsPy – What can it do for data centers and observatories? *Astron. Geophys.*, *54*(1). Retrieved from `http://doi.org/10.4401/ag-4838` doi: 10.4401/ag-4838

Melluso, L., Cucciniello, C., le Roex, A., & Morra, V. (2016). The geochemistry of primitive volcanic rocks of the Ankaratra volcanic complex, and source enrichment processes in the genesis of the Cenozoic magmatism in Madagascar. *Geochim. Cosmochim. Acta.*, *185*, 435–452. Retrieved from `https://doi.org/10.1016/j.gca.2016.04.005` doi: 10.1016/j.gca.2016.04.005

Mériaux, C., Duarte, J., Duarte, S., Schellart, W., Chen, Z., Rosas, F., ... Terrinha, P. (2015). Capture of the Canary mantle plume material by the Gibraltar arc mantle wedge during slab rollback. *Geophys. J. Int.*, *201*(3), 1717–1721. Retrieved from `https://doi.org/10.1093/gji/ggv120` doi: 10.1093/gji/ggv120

Michon, L. (2015). The volcanism of the Comoros Archipelago integrated at a regional scale. In *Active volcanoes of the southwest indian ocean* (pp. 333–344). Springer Berlin Heidelberg. Retrieved from `https://doi.org/10.1007/978-3-642-31395-0\_21` doi: 10.1007/978-3-642-31395-0_21

Milelli, L., Fourel, L., & Jaupart, C. (2012). A lithospheric instability origin for the Cameroon Volcanic Line. *Earth Planet. Sci. Lett.*, *335-336*, 80–87. Retrieved from `https://doi.org/10.1016/j.epsl.2012.04.028` doi: 10.1016/j.epsl.2012.04.028

Miller, M. S., O'Driscoll, L. J., Butcher, A. J., & Thomas, C. (2015). Imaging Canary Island hotspot material beneath the lithosphere of Morocco and southern Spain. *Earth Planet. Sci. Lett.*, *431*, 186–194. Retrieved from `https://doi.org/10.1016/j.epsl.2015.09.026` doi: 10.1016/j.epsl.2015.09.026

Missenard, Y., & Cadoux, A. (2011). Can Moroccan Atlas lithospheric thinning and volcanism be induced by edge-driven convection? *Terra Nova*, *24*(1), 27–33. Retrieved from `https://doi.org/10.1111/j.1365-3121.2011.01033.x` doi: 10.1111/j.1365-3121.2011.01033.x

Monaco, M., Dannberg, J., Gassmöller, R., & Pugh, S. (2022). The segregation of recycled basaltic material within mantle plumes explains the detection of the x-discontinuity beneath hotspots: 2d geodynamic simulations. *Earth and Space Science Open Archive*, 25. Retrieved from https://doi.org/10.1002/essoar.10512065.1 doi: 10.1002/essoar.10512065.1

Montigny, R., Ngounouno, I., & Déruelle, B. (2004). Âges KAr des roches magmatiques du fossé de garoua (cameroun) : leur place dans le cadre de la ≪ ligne du cameroun ≫. *C. R. Geosci.*, *336*(16), 1463–1471. Retrieved from https://doi.org/10.1016/j.crte.2004.08.005 doi: 10.1016/j.crte.2004.08.005

Muirhead, J. D., Fischer, T. P., Oliva, S. J., Laizer, A., van Wijk, J., Currie, C. A., … Ebinger, C. J. (2020). Displaced cratonic mantle concentrates deep carbon during continental rifting. *Nature*, *582*(7810), 67–72. Retrieved from https://doi.org/10.1038/s41586-020-2328-3 doi: 10.1038/s41586-020-2328-3

Mulibo, G. D., & Nyblade, A. A. A. (2016). The seismotectonics of Southeastern Tanzania: Implications for the propagation of the eastern branch of the East African Rift. *Tectonophysics*, *674*, 20–30. Retrieved from https://doi.org/10.1016/j.tecto.2016.02.009 doi: 10.1016/j.tecto.2016.02.009

Nyblade, A. A. (2000). *Seismic investigation of deep structure beneath the Ethiopian Plateau and Afar Depression.* International Federation of Digital Seismograph Networks. Retrieved from https://www.fdsn.org/networks/detail/XI_2000/ doi: 10.7914/SN/XI_2000

Nyblade, A. A. (2007). *Africa Array - Uganda/Tanzania.* International Federation of Digital Seismograph Networks. Retrieved from https://www.fdsn.org/networks/detail/ZP_2007/ doi: 10.7914/SN/ZP_2007

Nyblade, A. A. (2010). *AfricaArray SE Tanzania Basin Experiment.* International Federation of Digital Seismograph Networks. Retrieved from https://www.fdsn.org/networks/detail/YH_2010/ doi: 10.7914/SN/YH_2010

Nyblade, A. A. (2015a). *AfricaArray - Namibia.* IRIS. Retrieved from https://www.fdsn.org/networks/detail/8A_2015/ doi: 10.7914/SN/8A_2015

Nyblade, A. A. (2015b). *REU: Imaging the Bushveld Complex, South Africa.* International Federation of Digital Seismograph Networks. Retrieved from https://www.fdsn.org/networks/detail/ZT_2015/ doi: 10.7914/SN/ZT_2015

Nyblade, A. A. (2017). *Broadband seismic experiment in NE Uganda to investigate plume-lithosphere interactions.* International Federation of Digital Seismograph Networks. Retrieved from https://www.fdsn.org/networks/detail/XW_2017 doi: 10.7914/SN/XW_2017

Observatoire Volcanologique Du Piton De La Fournaise (OVPF), & Institut De Physique Du Globe De Paris (IPGP). (2008). *Seismic, tiltmeter, extensometer, magnetic and weather permanent networks on Piton de la Fournaise volcano and La Réunion.* Institut de physique du globe de Paris (IPGP), Université de Paris. Retrieved from http://volobsis.ipgp.fr/networks/detail/PF doi: 10.18715/REUNION.PF

O'Connor, J. M., Jokat, W., Regelous, M., Kuiper, K. F., Miggins, D. P., & Koppers, A. A. P. (2019). Superplume mantle tracked isotopically the length of Africa from the Indian Ocean to the Red Sea. *Nat. Commun.*, *10*(1). Retrieved from https://doi.org/10.1038/s41467-019-13181-7 doi: 10.1038/s41467-019-13181-7

Owens, T. J., & Nyblade, A. A. (1994). *Seismic investigations of the lithospheric structure of the Tanzanian Craton.* International Federation of Digital Seismograph Networks. Retrieved from https://www.fdsn.org/networks/detail/XD_1994/ doi: 10.7914/SN/XD_1994

Owens, T. J., Nyblade, A. A., Gurrola, H., & Langston, C. A. (2000). Mantle transition zone structure beneath Tanzania, East Africa. *Geophys. Res. Lett.*, *27*(6), 827–830. Retrieved from https://doi.org/10.1029/1999GL005429 doi: 10.1029/1999GL005429

Penn State University. (2004). *AfricaArray.* International Federation of Digital Seismograph Networks. Retrieved from https://www.fdsn.org/networks/detail/AF/ doi: 10.7914/SN/AF

Pik, R., Marty, B., & Hilton, D. (2006). How many mantle plumes in Africa? The geochemical point of view. *Chem. Geol.*, *226*(3-4), 100–114. Retrieved from https://doi.org/10.1016/j.chemgeo.2005.09.016 doi: 10.1016/j.chemgeo.2005.09.016

Priestley, K., McKenzie, D., Debayle, E., & Pilidou, S. (2008). The African upper mantle and its relationship to tectonics and surface geology. *Geophys. J. Int.*, *175*(3), 1108–1126. Retrieved from https://doi.org/10.1111/j.1365-246x

.2008.03951.x doi: 10.1111/j.1365-246x.2008.03951.x

Priestley, K., McKenzie, D., & Ho, T. (2018). A lithosphere–asthenosphere boundary—A global model derived from multimode surface-wave tomography and petrology. *Lithospheric discontinuities*, 111–123. Retrieved from https://doi.org/10.1002/9781119249740.ch6 doi: 10.1002/9781119249740.ch6

Pugh, S., Jenkins, J., Boyce, A., & Cottaar, S. (2021). Global receiver function observations of the X-discontinuity reveal recycled basalt beneath hotspots. *Earth Planet. Sci. Lett.*, *561*, 116813. Retrieved from https://doi.org/10.1016/j.epsl.2021.116813 doi: 10.1016/j.epsl.2021.116813

Rakhmanov, E. A., Saff, E. B., & Zhou, Y. (1994). Minimal discrete energy on the sphere. *Math. Res. Lett.*, *1*(6), 647–662. Retrieved from https://dx.doi.org/10.4310/MRL.1994.v1.n6.a3 doi: 10.4310/MRL.1994.v1.n6.a3

Reed, C., Gao, S., Liu, K., & Yu, Y. (2016). The mantle transition zone beneath the Afar Depression and adjacent regions: implications for mantle plumes and hydration. *Geophys. J. Int.*, *205*(3), 1756–1766. Retrieved from https://doi.org/10.1093/gji/ggw116 doi: 10.1093/gji/ggw116

Rein, T., Hannemann, K., Thomas, C., & Korn, M. (2020). Location and characteristics of the X-discontinuity beneath SW Morocco and the adjacent shelf area using P-wave receiver functions. *Geophys. J. Int.*, *223*(3), 1780–1793. Retrieved from https://doi.org/10.1093/gji/ggaa379 doi: 10.1093/gji/ggaa379

Reusch, A. M., Nyblade, A. A., Tibi, R., Wiens, D. A., Shore, P. J., Bekoa, A., … Nnange, J. M. (2011). Mantle transition zone thickness beneath Cameroon: evidence for an upper mantle origin for the Cameroon Volcanic Line. *Geophys. J. Int.*, *187*(3), 1146–1150. Retrieved from https://doi.org/10.1111/j.1365-246x.2011.05239.x doi: 10.1111/j.1365-246x.2011.05239.x

Reusch, A. M., Nyblade, A. A., Wiens, D. A., Shore, P. J., Ateba, B., Tabod, C. T., & Nnange, J. M. (2010). Upper mantle structure beneath Cameroon from body wave tomography and the origin of the Cameroon Volcanic Line. *Geochem. Geophys. Geosyst.*, *11*(10), n/a–n/a. Retrieved from https://doi.org/10.1029/2010gc003200 doi: 10.1029/2010gc003200

Revenaugh, J., & Jordan, T. H. (1991). Mantle layering from ScS reverberations: 3. the upper mantle. *J. Geophys. Res. Solid Earth*, *96*(B12), 19781–19810. Retrieved from https://doi.org/10.1029/91jb01487 doi: 10.1029/91jb01487

Ritsema, J., Deuss, A., van Heijst, H. J., & Woodhouse, J. H. (2010). S40rts: a degree-40 shear-velocity model for the mantle from new Rayleigh wave dispersion, teleseismic traveltime and normal-mode splitting function measurements. *Geophys. J. Int.*, *184*(3), 1223–1236. Retrieved from https://doi.org/10.1111/j.1365-246x.2010.04884.x doi: 10.1111/j.1365-246x.2010.04884.x

Ritsema, J., van Heijst, H., & Woodhouse, J. (1999). Complex shear wave velocity structure imaged beneath Africa and Iceland. *Science*, *286*, 1925-1928.

Roberts, E. M., Stevens, N. J., O'Connor, P. M., Dirks, P. H. G. M., Gottfried, M. D., Clyde, W. C., … Hemming, S. (2012). Initiation of the western branch of the East African Rift coeval with the eastern branch. *Nat. Geosci.*, *5*(4), 289–294. Retrieved from https://doi.org/10.1038/ngeo1432 doi: 10.1038/ngeo1432

Rooney, T. O. (2017). The Cenozoic magmatism of East-Africa: Part I–Flood basalts and pulsed magmatism. *Lithos*, *286-287*, 264–301. Retrieved from https://doi.org/10.1016/j.lithos.2017.05.014 doi: 10.1016/j.lithos.2017.05.014

Rooney, T. O., Herzberg, C., & Bastow, I. D. (2012). Elevated mantle temperature beneath East Africa. *Geology*, *40*(1), 27–30. Retrieved from https://doi.org/10.1130/g32382.1 doi: 10.1130/g32382.1

Saki, M., Thomas, C., Nippress, S. E., & Lessing, S. (2015). Topography of upper mantle seismic discontinuities beneath the North Atlantic: The Azores, Canary and Cape Verde plumes. *Earth Planet. Sci. Lett.*, *409*, 193–202. Retrieved from https://doi.org/10.1016/j.epsl.2014.10.052 doi: 10.1016/j.epsl.2014.10.052

San Fernando Royal Naval Observatory (ROA), Universidad Complutense De Madrid (UCM), Helmholtz-Zentrum Potsdam Deutsches GeoForschungsZentrum (GFZ), Universidade De Evora (UEVORA, Portugal), & Institute Scientifique Of RABAT (ISRABAT, Morocco). (1996). *The Western Mediterranean BB seismic Network.* Deutsches GeoForschungsZentrum GFZ. Retrieved from http://geofon.gfz-potsdam.de/doi/network/WM doi: 10.14470/JZ581150

Schaeffer, A. J., & Lebedev, S. (2013). Global shear speed structure of the upper mantle and transition zone. *Geophys. J. Int.*, *194*(1), 417–449. Retrieved from https://doi.org/10.1093/gji/ggt095 doi: 10.1093/gji/ggt095

Schaeffer, A. J., & Lebedev, S. (2014). Imaging the North American continent using waveform inversion of global and USArray data. *Earth Planet. Sci. Lett.*, *402*, 26–41. Retrieved from https://doi.org/10.1016/j.epsl.2014.05.014 doi: 10.1016/j.epsl.2014.05.014

Schmerr, N. (2015). Imaging mantle heterogeneity with upper mantle seismic discontinuities. In *The earth's heterogeneous mantle* (pp. 79–104). Springer International Publishing. Retrieved from https://doi.org/10.1007/978-3-319-15627-9_3 doi: 10.1007/978-3-319-15627-9_3

Schmerr, N., Kelly, B. M., & Thorne, M. S. (2013). Broadband array observations of the 300 km seismic discontinuity. *Geophys. Res. Lett.*, *40*(5), 841–846. Retrieved from https://doi.org/10.1002/grl.50257 doi: 10.1002/grl.50257

Scripps Institution of Oceanography. (1986). *Global Seismograph Network - IRIS/IDA.* International Federation of Digital Seismograph Networks. Retrieved from https://www.fdsn.org/networks/detail/II/ doi: 10.7914/SN/II

Silver, P. (1997). *Anatomy of an Archean Craton, South Africa, A Multidisciplinary Experiment across the Kaapvaal Craton.* International Federation of Digital Seismograph Networks. Retrieved from https://www.fdsn.org/networks/detail/XA_1997/ doi: 10.7914/SN/XA_1997

Simmons, N. A., Forte, A. M., & Grand, S. P. (2007). Thermochemical structure and dynamics of the African superplume. *Geophys. Res. Lett.*, *34*(2). Retrieved from https://doi.org/10.1029/2006gl028009 doi: 10.1029/2006gl028009

Sodoudi, F., Yuan, X., Kind, R., Lebedev, S., Adam, J. M.-C., Kästle, E., & Tilmann, F. (2013). Seismic evidence for stratification in composition and anisotropic fabric within the thick lithosphere of kalahari craton. *Geochem. Geophys. Geosyst.*, *14*(12), 5393–5412. Retrieved from https://doi.org/10.1002/2013gc004955 doi: 10.1002/2013gc004955

Tepp, G., Ebinger, C. J., Zal, H., Gallacher, R., Accardo, N., Shillington, D. J., … Kamihanda, G. (2018). Seismic anisotropy of the upper mantle below the western rift, east africa. *J. Geophys. Res. Solid Earth*, *123*(7), 5644–5660. Retrieved from https://doi.org/10.1029/2017jb015409 doi: 10.1029/2017jb015409

The ARGOS Project. (2012). *ARGOS - Alutu and regional geophysical observation study.* International Federation of Digital Seismograph Networks. Retrieved from https://www.fdsn.org/networks/detail/XM_2012/ doi: 10.7914/SN/XM_2012

Thirlwall, M. (1997). Pb isotopic and elemental evidence for OIB derivation from young HIMU mantle. *Chem. Geol.*, *139*(1-4), 51–74. Retrieved from https://doi.org/10.1016/s0009-2541(97)00033-8 doi: 10.1016/s0009-2541(97)00033-8

Thomas, C. (2010). *Morocco-muenster.* International Federation of Digital Seismograph Networks. Retrieved from https://www.fdsn.org/networks/detail/3D_2010/ doi: 10.7914/SN/3D_2010

Thompson, D. A., Hammond, J. O. S., Kendall, J.-M., Stuart, G. W., Helffrich, G. R., Keir, D., . . . Goitom, B. (2015). Hydrous upwelling across the mantle transition zone beneath the Afar Triple Junction. *Geochem. Geophys. Geosyst.*, *16*(3), 834–846. Retrieved from https://doi.org/10.1002/2014gc005648 doi: 10.1002/2014gc005648

Thompson, D. A., Helffrich, G., Bastow, I., Kendall, J.-M., Wookey, J., Eaton, D., & Snyder, D. (2011). Implications of a simple mantle transition zone beneath cratonic North America. *Earth Planet. Sci. Lett.*, *312*(1-2), 28–36. Retrieved from https://doi.org/10.1016/j.epsl.2011.09.037 doi: 10.1016/j.epsl.2011.09.037

Tilmann, F., Yuan, X., Rümpker, G., & Rindraharisaona, E. (2012). *SELASOMA Project, Madagascar 2012-2014.* GFZ Data Services. Retrieved from http://geofon.gfz-potsdam.de/doi/network/ZE/2012 doi: 10.14470/MR7567431421

Tsekhmistrenko, M., Sigloch, K., Hosseini, K., & Barruol, G. (2021). A tree of Indo-African mantle plumes imaged by seismic tomography. *Nat. Geosci.*, *14*(8), 612–619. Retrieved from https://doi.org/10.1038/s41561-021-00762-9 doi: 10.1038/s41561-021-00762-9

Utrecht University (UU Netherlands). (1983). *NARS.* International Federation of Digital Seismograph Networks. Retrieved from https://www.fdsn.org/networks/detail/NR/ doi: 10.7914/SN/NR

van den Bogaard, P. (2013). The origin of the Canary Island Seamount Province -

New ages of old seamounts. *Sci. Rep.*, *3*(1). Retrieved from https://doi.org/10.1038/srep02107 doi: 10.1038/srep02107

van der Lee, S., Deschamps, A., Margheriti, L., & Giardini, D. (1999). *Midsea - mantle investigation of the deep suture between Eurasia and Africa.* International Federation of Digital Seismograph Networks. Retrieved from https://www.fdsn.org/networks/detail/YF_1999/ doi: 10.7914/SN/YF_1999

van Stiphout, A. M., Cottaar, S., & Deuss, A. (2019). Receiver function mapping of mantle transition zone discontinuities beneath Alaska using scaled 3-D velocity corrections. *Geophys. J. Int.*, *219*(2), 1432–1446. Retrieved from https://doi.org/10.1093/gji/ggz360 doi: 10.1093/gji/ggz360

Velasco, A., Kaip, G., Wamalwa, A., & Patlan, E. (2011). *Seismic characterization of menengai crater, kenya.* International Federation of Digital Seismograph Networks. Retrieved from https://www.fdsn.org/networks/detail/1C_2011/ doi: 10.7914/SN/1C_2011

Vergne, J., Doubre, C., & Leroy, S. (2014). *Seismic network 7c:dora experiment (resif-sismob).* RESIF - Réseau Sismologique et géodésique Français. Retrieved from https://seismology.resif.fr/networks/#/7C__2009 doi: 10.15778/RESIF.7C2009

Weber, M., Silveira, G., & Schulze, A. (2007). *The COBO/CV-PLUME temporary seismic network.* GFZ Data Services. Retrieved from https://geofon.gfz-potsdam.de/doi/network/9A/2007 doi: 10.14470/4N7552467332

Widom, E., Hoernle, K. A., Shirey, S. B., & Schmincke, H.-U. (1999). Os isotope systematics in the Canary Islands and Madeira: Lithospheric contamination and mantle plume signatures. *J. Petrol.*, *40*(2), 279–296. Retrieved from https://doi.org/10.1093/petroj/40.2.279 doi: 10.1093/petroj/40.2.279

Wiens, D., & Nyblade, A. A. (2005). *Broadband Seismic Investigation of the Cameroon Volcanic Line.* International Federation of Digital Seismograph Networks. Retrieved from https://www.fdsn.org/networks/detail/XB_2005/ doi: 10.7914/SN/XB_2005

Williams, C. D., Mukhopadhyay, S., Rudolph, M. L., & Romanowicz, B. (2019). Primitive helium is sourced from seismically slow regions in the lowermost mantle. *Geochem. Geophys. Geosyst.*, *20*(8), 4130–4145. Retrieved from https://doi.org/10.1029/2019gc008437 doi: 10.1029/2019gc008437

Williams, Q., & Revenaugh, J. (2005). Ancient subduction, mantle eclogite, and the 300 km seismic discontinuity. *Geology*, *33*(1), 1. Retrieved from https://doi.org/10.1130/g20968.1 doi: 10.1130/g20968.1

Wölbern, I., Rümpker, G., Link, K., & Sodoudi, F. (2012). Melt infiltration of the lower lithosphere beneath the tanzania craton and the albertine rift inferred from s receiver functions. *Geochem. Geophys. Geosyst.*, *13*(8), n/a–n/a. Retrieved from https://doi.org/10.1029/2012gc004167 doi: 10.1029/2012gc004167

Woodland, A. B. (1998). The orthorhombic to high-P monoclinic phase transition in Mg-Fe pyroxenes: Can it produce a seismic discontinuity? *Geophys. Res. Lett.*, *25*(8), 1241–1244. Retrieved from https://doi.org/10.1029/98gl00857 doi: 10.1029/98gl00857

Wookey, J., Horleston, A., Leo, J. D., Thomas, C., Harnafi, M., & Elouai, D. (2011). *CoMITAC Morocco-Bristol Network.* International Federation of Digital Seismograph Networks. Retrieved from https://www.fdsn.org/networks/detail/ZI_2011/ doi: 10.7914/SN/ZI_2011

Woolley, A. R., & Kjarsgaard, B. A. (2008). *Carbonatite occurrences of the world.* Geological Survey of Canada.

Wysession, M., Wiens, D., & Nyblade, A. A. (2011). *Investigation of sources of intraplate volcanism using passcal broadband instruments in Madagascar, the Comores, and Mozambique.* International Federation of Digital Seismograph Networks. Retrieved from https://www.fdsn.org/networks/detail/XV_2011/ doi: 10.7914/SN/XV_2011

Xu, F., Vidale, J. E., Earle, P. S., & Benz, H. M. (1998). Mantle discontinuities under southern Africa from precursors to $P'P'_{df}$. *Geophys. Res. Lett.*, *25*(4), 571–574. Retrieved from https://doi.org/10.1029/98GL00122 doi: 10.1029/98GL00122

Supporting Information for "Multigenetic Origin of the X-discontinuity Below Continents: Insights from African Receiver Functions"

Stephen Pugh[1*], Alistair Boyce[1,2], Ian D. Bastow[3], C. J. Ebinger[4], Sanne Cottaar[1]

[1]Bullard Laboratories, Department of Earth Sciences, University of Cambridge, UK

[2]Université Lyon 1, ENS de Lyon, CNRS, UMR 5276 LGL-TPE, F-69622, Villeurbanne, France

[3]Department of Earth Science and Engineering, Imperial College, London, UK

[4]Department of Earth and Environmental Sciences, Tulane University, New Orleans, LA, USA

*Corresponding author: Stephen Pugh, sdp43@cam.ac.uk

Contents of this file

1 Introduction

This supplement provides supporting figures and details to the main text. Section 2 provides the sources of sources data without corresponding DOIs in Table S1. Seismic networks with DOIs are detailed in the Open Research section of the main article. Section 3 gives an overview of manual quality control procedures implement post automatic quality control. Section 4 considers the data distribution of RF stacks and its impact on the quality of the stack. Section 5 assesses the different time-to-depth conversions implemented before stacking. Section 6 considers the relationship between presence of the X and the local temperature of the upper mantle for each stack. Finally, Section 7 considers the relationship between the X and lithospheric thickness for the vote map in Figure 5.

2 Seismic Networks for P-wave Receiver Functions in Africa

Network	FDSN website address
1B	http://www.fdsn.org/networks/detail/1B_2006/
BX	http://www.fdsn.org/networks/detail/BX/
TT	http://www.fdsn.org/networks/detail/TT/
XJ	http://www.fdsn.org/networks/detail/XJ_2002/
XJ	http://www.fdsn.org/networks/detail/XJ_2007/
XM	http://www.fdsn.org/networks/detail/XM_2002/
YF	http://www.fdsn.org/networks/detail/YF_2010/
YJ	http://www.fdsn.org/networks/detail/YJ_2001/
YK	http://www.fdsn.org/networks/detail/YK_2000/
YW	http://www.fdsn.org/networks/detail/YW_2002/
YZ	http://www.fdsn.org/networks/detail/YZ_2005/
ZC	http://www.fdsn.org/networks/detail/ZC_2001/
ZF	http://www.fdsn.org/networks/detail/ZF_2007/
ZP	http://www.fdsn.org/networks/detail/ZP_2010/
ZQ	http://www.fdsn.org/networks/detail/ZQ_2006/
ZU	http://www.fdsn.org/networks/detail/ZU_2008/

Table 1. Data for this project were downloaded for a range of networks using the Incorporated Research Institutions for Seismology (IRIS) Data Management System. The networks used with associated DOIs are detailed in the Open Research section of the main article. Those listed here do not have associated DOIs and their corresponding websites are written alongside.

Table S1 shows seismic networks used to record the P wave RFs in this study without a corresponding DOI are found in Table 1. Seismic networks with a corresponding DOI are detailed in the Open Research section of the main article.

3 Manual Quality Control

Manual quality control involves visual inspection of RFs accepted by automatic quality control to identify low quality RFs clearly contaminated by long-wavelength noise (Figure 1). The source of this noise appears only on the radial component seismogram,

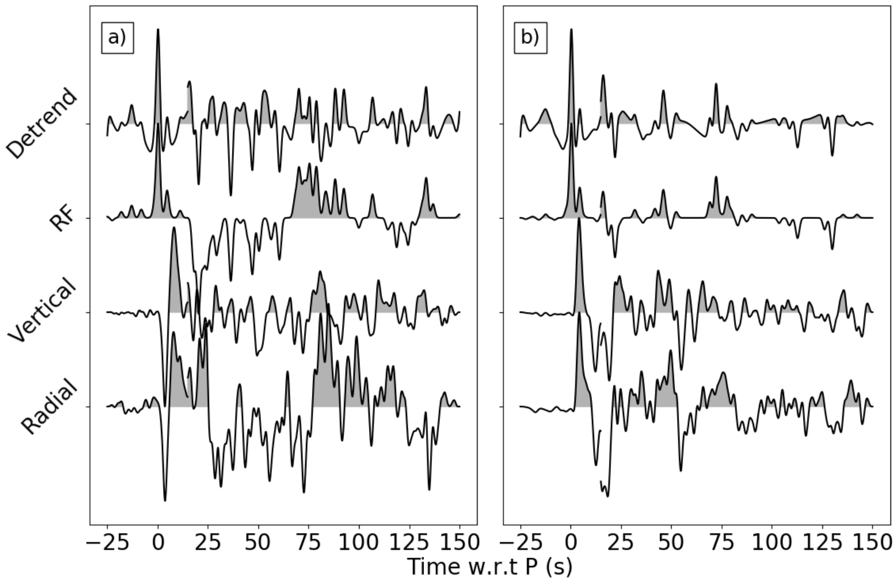

Figure 1. A poor quality (a) and accepted (b) receiver function (RF) identified by visual inspection with the corresponding vertical and radial component seismograms filtered to 0.01-0.4 Hz and the same RF detrended using a 5^{th} order spline. All traces are amplified by a factor of 3 between 15-150 s.

but is not constrained to any particular seismic stations. Whilst a 4^{th} or 5^{th} order sinusoidal spline is capable of removing the long wavelength noise from these RFs, higher frequency noise remains that is indistinguishable from the seismic signals of interest. RFs are only removed where clear high amplitude noise is present, affecting ∼10% of RFs that pass automatic quality control.

4 Data Distribution

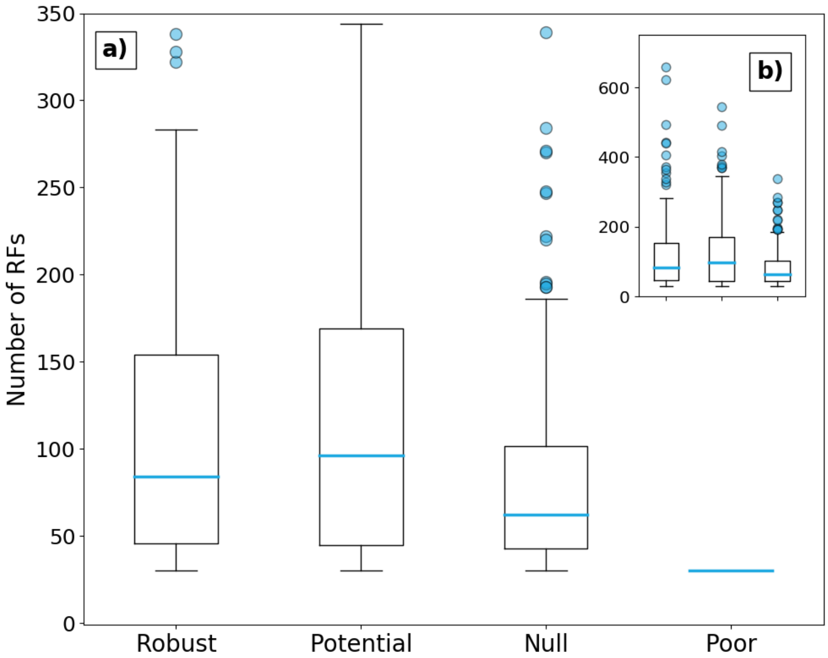

Figure 2. Box plots of the number of RFs for each classification of stack in Figure 5 with a) zoomed to show all non-outlying values and b) showing the full range of the data. The blue line represents the median number of receiver functions for each classification, with the box extending from the 25^{th} to the 75^{th} percentile. Outliers are marked with blue circles.

Using a large data set presents the opportunity to study the impact of data distribution on the resulting stacks and maps. Here we consider the impact of the number of RFs, and the epicentral distance and backazimuthal distance distribution of RFs.

Reassuringly, the number of RFs in a stack has little bearing on the classification of the stacks with robust, potential and null stacks having median values of 84 RFs, 96.5 RFs, and 62.5 RFs respectively. It can also be seen that there is significant overlap in the interquartile range for each classification of stack (Figure 2). Comparison is not made to the sole poor quality stack.

Backazimuth standard deviation is a measure of the spread of backazimuths for a single stack, calculated using the circular standard deviation. When comparing the presence of phases in the depth range for the X (depth stack only) and the standard deviation of backazimuth (σ) in Figure 3, it is apparent that the two are anti-correlated. Though this anti-correlation is weak (ρ = -0.42), it can be seen in several regions that a reduction in σ is accompanied by an increase in normalised vote for arrivals in the depth range of PXs and is as great as -0.64 for Madagascar and the Indian Ocean region. There are two potential causes of this anti-correlation: topography on the X, and/or the influence of epicentral distance distribution.

If topography exists on the X, then stacks with small standard deviation in backazimuth are less likely to be sensitive to this, especially if stacks are dominated by arrivals at one station. Using stacks with large numbers of RFs ($\geq$100), RFs can be subdivided into four quadrants of backazimuth (Figure 4) to analyse whether topography occurs across the X. Finding the circular mean, four quadrants can be designated such that the dominant backazimuth of data is not divided into multiple bins (Figure 4a). For most RF stacks, this results in one quadrant with most RFs, and three others with few to none, thus being unusable for this analysis. Figure 4 shows an example with sufficient data in more than one bin (Figures 4d-g, j and k). Stacking all RFs for this bin shows an X arrival (Figures 4b and c), though it is somewhat streaky with data looking to have come from epicentral distances >70°. Splitting the stack into four quadrants reveals a high quality X observation in data approximately from the East (Figures 4f and g) at 276 km depth, two potential X observations in data from the north (Figures 4d and e) and west (Figures 4j and k) at 281 and 297 km depth and a poor quality stack with data from the south (Figures 4h and i). It is clear the overall stack (Figures 4b and c) is dominated by data from the west (Figures 4j and k) with >70% of RFs coming from this backazimuthal quadrant which shows the streaky X arrival at 297 km depth. While the data from the west (Figures 4j and k) would be classified as 'Potential' if taken alone, comparison with data from the East (Figures 4f and g) show that >20 km of topography may occur across the stacking regions should this streaky arrival be taken to be the X. This stack also highlights the potential for X observations to be masked by data predominantly sourced from a small epicentral distance range. Epicentral distance distribution is strongly

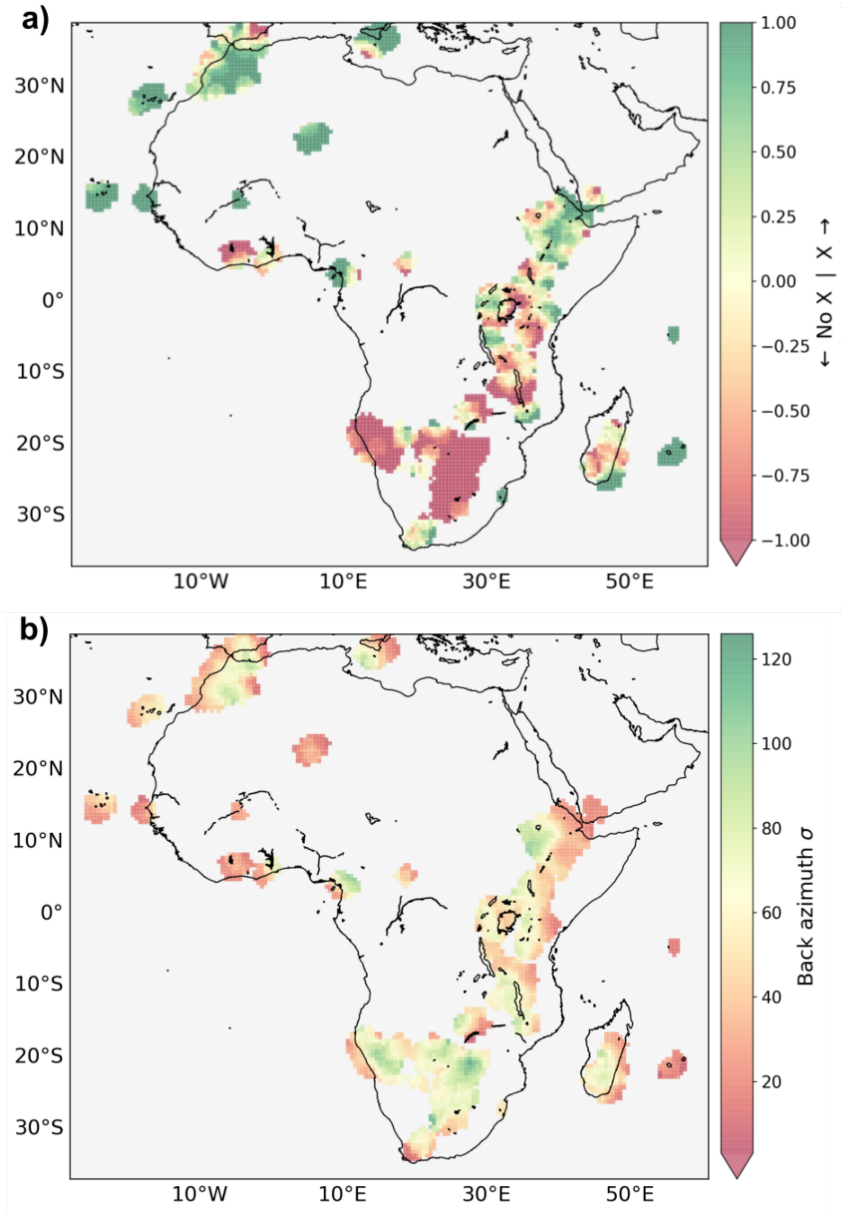

Figure 3. Vote maps of a) X observation in depth stacks and b) standard deviation of backazimuth (σ) for 597 overlapping 1° radius bins with ≥2 votes on a 0.5°x0.5° grid.

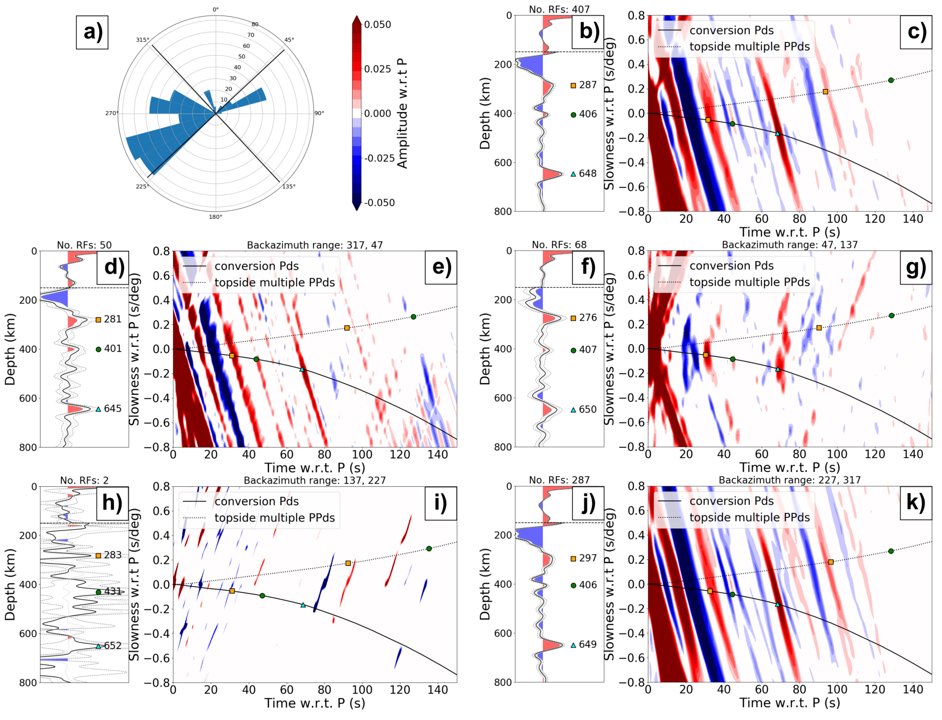

Figure 4. a) Backazimuth distribution of RFs within one bin. Depth (b, d, f, h and j and slowness (c, e, g, i and k) stacks of all data for one bin (b and c) and four quadrants of backazimuth (d-k) as divided by the thick black lines in a). Stacks are filtered between 0.01-0.4 Hz. Depth stack: Time-to-depth converted RFs are linearly stacked with the black line marking amplitude (normalised to P) and dashed lines marking 2 σ_M. Amplitudes are multiplied by 5 below the horizontal dashed line at 150 km depth. The stack is converted from time-to-depth using SEMUCB_WM1. Coloured symbols mark significant peaks from PXs (orange squares), P410s (green circles), and P660s (cyan triangles). Slowness stack: RFs with amplitude >2 σ_M normalised to P stacked in the time-slowness domain. Predicted time-slowness curves are shown for the direct (Pds) and multiple (PPvds) phases. The coloured symbols correspond to predicted times and slownesses for direct arrivals and PPvds multiples for significant arrivals in the depth stacks computed from PREM.

linked with backazimuth distribution. As for a single backazimuth, it is likely there are only a narrow range of epicentral distances where earthquakes occur due to the sparsity of plate boundaries across Earth's surface.

5 Time-to-depth Conversion

To assess the quality of time-to-depth conversions, receiver function studies often assess the (de-)correlation between 410 and 660 km discontinuity depths (e.g. Dueker & Sheehan, 1998; van Stiphout et al., 2019; Boyce & Cottaar, 2021). Given the polarity of the Clapeyron slopes for the 410 and 660, and assuming the mantle transition zone is dominated by temperature variations, the topography on the 410 and 660 is largely expected to be anti-correlated in the olivine system. Unaccounted for structures in the upper mantle would consistently shift both the 410 and 660 up or down with equal magnitude for fast and slow wavespeed anomalies respectively. A reduction in correlation between 410 km and 660 km topography is used as evidence that a velocity model better accounts for upper mantle velocity structure. The maximum topography and the distribution of topography are also considered to assess how well PREM, SEMUCB_WM1 and AF2019 correct for velocity structure in the African upper mantle.

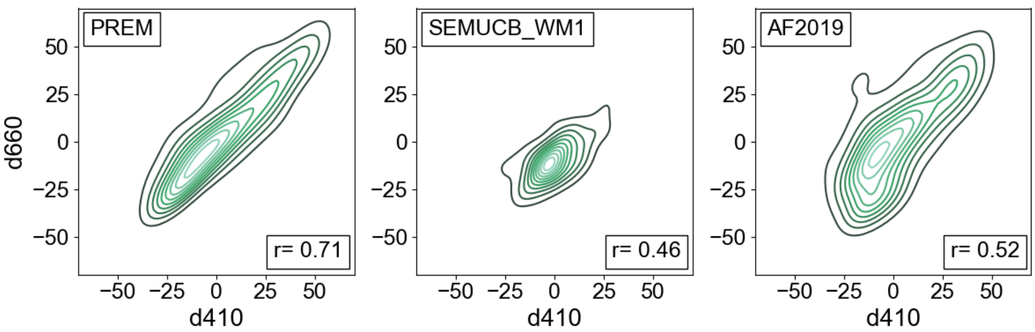

Figure 5. Probability density plots of 410 and 660 km topography for 597 RF stacks depth converted using PREM, SEMUCB_WM1 and AF2019. d410 and d660 are the topography in each stack taken with respect to 410 and 660 km. Pearson's r correlation values are displayed in the bottom right for each model.

1D velocity models are not expected to account for upper mantle heterogeneities and this can be seen in Figure 5 where the d410 and d660 values are strongly correlated with a Pearson's correlation coefficient of 0.71 and >100 km topography on both the 410 and 660. SEMUCB_WM1 shows the lowest correlation (r=0.46) of the three velocity models suggesting it best accounts for upper mantle velocity structure and can be seen to have the least linear probability density ellipses (Figure 5). Though the correlation of AF2019 (r=0.52) is similar to that from SEMUCB_WM1, topography on both discontinuities is much larger.

The Clapeyron slope of the MTZ discontinuities can be used to estimate total temperature variations across a region. 410 km topography is preferred for this probe as 660 km depths are sensitive to temperature and composition (e.g. Jenkins et al., 2016). Considering an average Clapeyron slope of the 410 km discontinuity of 2.5 MPa/K (Katsura & Ito, 1989; Bina & Helffrich, 1994), the 108 km topography found between stacks using AF2019 would lead to a maximum temperature variation of 1600 K across the region, far greater than the combined temperature anomalies of cold slabs (200-300 K; Cottaar & Deuss, 2016) and hot plumes (150-200 K; Matthews et al., 2016) in the mantle. For the total topography of 76 km between stacks using SEMUCB_WM1, the maximum temperature variation is found to be 1100 K. Although this temperature variation is still larger than expected, SEMUCB_WM1 is preferred for depth correction as temperature variation and topography suggest it better accounts for upper mantle velocity structure. Subsequently, depths reported below are as converted using SEMUCB_WM1.

6 Average upper mantle temperatures of RF stacks

We calculate average upper mantle temperatures between 200-400 km depth for every stack $\pm 1°$ latitude and longitude using the temperature deviations found in a geophysical-petrological inversion (Fullea et al., 2021). Histograms in Figure 6 show that Robust observations, distributed across the entire temperature range, are no more likely at elevated mantle temperature than depressed mantle temperatures. However, Null observations are more readily observed at depressed mantle temperatures, potentially linked with widespread Null observations beneath the Kalahari Craton.

7 X-discontinuity relationship to lithospheric thickness

Hoggard et al. (2020) derive lithospheric thickness maps for several tomographic models. Figure 7 shows the distribution of lithospheric thicknesses for three tomographic models SLNAAFSA (A. J. Schaeffer & Lebedev, 2013; A. Schaeffer & Lebedev, 2014;

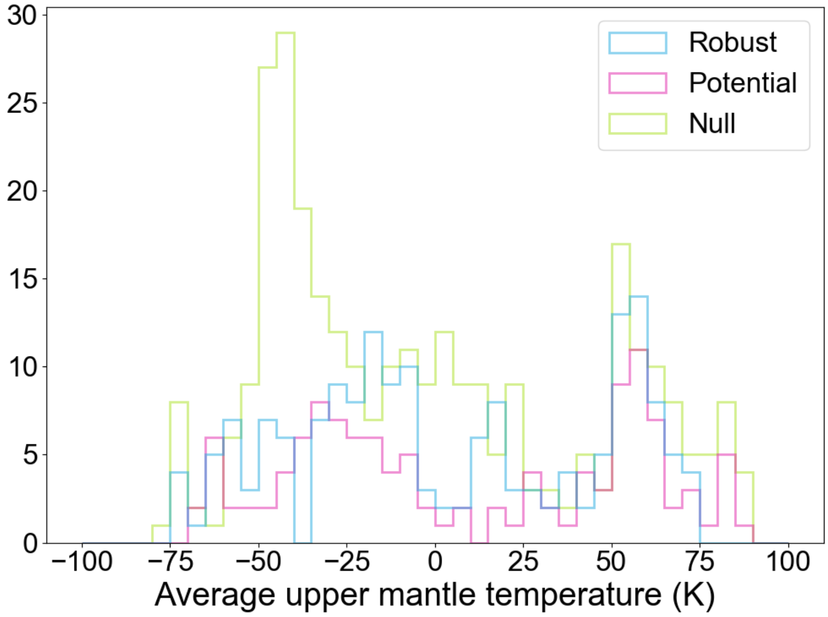

Figure 6. Histograms of the average upper mantle temperature deviations between 200-400 km depth (Fullea et al., 2021) for Robust, Potential and Null stacks.

Celli, Lebedev, Schaeffer, & Gaina, 2020; Celli, Lebedev, Schaeffer, Ravenna, & Gaina, 2020), CAM2016 (Ho et al., 2016; Priestley et al., 2018) and 3D2015-sv (Debayle et al., 2016), for votes corresponding approximately to Robust, Potential and Null categorisations. Votes $\geq$ 0.5 are mostly clustered beneath lithospheric thicknesses of $\leq$ 100 km and almost entirely below 200 km, whereas votes $\leq$ -0.5 have maximum concentrations at thicknesses $\geq$ 120 km with some thicknesses $\geq$ 200 km for SLNAAFSA.

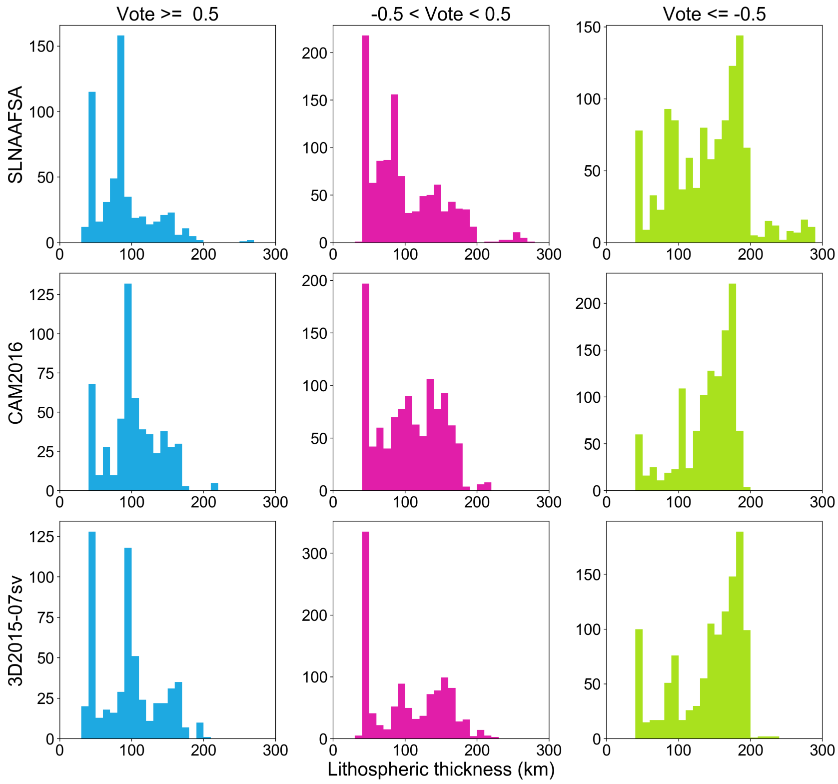

Figure 7. Histograms of the lithospheric thickness in each bin of the vote map (Figure 5) separated into votes for likely X-discontinuity (Vote $\geq$ 0.5), unclear (-0.5 $<$ Vote $<$ 0.5), and likely no X-discontinuity (Vote $\leq$ -0.5) for lithospheric thickness maps derived by Hoggard et al. (2020) from three tomographic models SLNAAFSA (A. J. Schaeffer & Lebedev, 2013; A. Schaeffer & Lebedev, 2014; Celli, Lebedev, Schaeffer, & Gaina, 2020; Celli, Lebedev, Schaeffer, Ravenna, & Gaina, 2020), CAM2016 (Ho et al., 2016; Priestley et al., 2018) and 3D2015-sv (Debayle et al., 2016).

References

Bina, C. R., & Helffrich, G. (1994). Phase transition Clapeyron slopes and transition zone seismic discontinuity topography. *J. Geophys. Res. Solid Earth*, *99*(B8), 15853. Retrieved from https://doi.org/10.1029/94jb00462 doi: 10.1029/94jb00462

Boyce, A., & Cottaar, S. (2021, March). Insights into deep mantle thermochemical contributions to African magmatism from converted seismic phases. *Geochem. Geophys. Geosyst.*, *22*(3). Retrieved from https://doi.org/10.1029/2020gc009478 doi: 10.1029/2020gc009478

Celli, N. L., Lebedev, S., Schaeffer, A. J., & Gaina, C. (2020, January). African cratonic lithosphere carved by mantle plumes. *Nat. Commun.*, *11*(1). Retrieved from https://doi.org/10.1038/s41467-019-13871-2 doi: 10.1038/s41467-019-13871-2

Celli, N. L., Lebedev, S., Schaeffer, A. J., Ravenna, M., & Gaina, C. (2020, January). The upper mantle beneath the South Atlantic Ocean, South America and Africa from waveform tomography with massive data sets. *Geophys. J. Int.*, *221*(1), 178–204. Retrieved from https://doi.org/10.1093/gji/ggz574 doi: 10.1093/gji/ggz574

Cottaar, S., & Deuss, A. (2016, January). Large-scale mantle discontinuity topography beneath Europe: Signature of akimotoite in subducting slabs. *J. Geophys. Res. Solid Earth*, *121*(1), 279–292. Retrieved from https://doi.org/10.1002/2015jb012452 doi: 10.1002/2015jb012452

Debayle, E., Dubuffet, F., & Durand, S. (2016). An automatically updated s-wave model of the upper mantle and the depth extent of azimuthal anisotropy. *Geophys. Res. Lett.*, *43*(2), 674–682.

Dueker, K. G., & Sheehan, A. F. (1998, April). Mantle discontinuity structure beneath the colorado rocky mountains and high plains. *J. Geophys. Res. Solid Earth*, *103*(B4), 7153–7169. Retrieved from https://doi.org/10.1029/97jb03509 doi: 10.1029/97jb03509

Fullea, J., Lebedev, S., Martinec, Z., & Celli, N. L. (2021, March). WINTERC-g: mapping the upper mantle thermochemical heterogeneity from coupled geophysical-petrological inversion of seismic waveforms, heat flow, surface elevation and gravity satellite data. *Geophys. J. Int.*, *226*(1), 146–191. Retrieved from https://doi.org/10.1093/gji/ggab094 doi: 10.1093/gji/ggab094

Ho, T., Priestley, K., & Debayle, E. (2016, August). A global horizontal shear velocity model of the upper mantle from multimode love wave measurements. *Geophys. J. Int.*, *207*(1), 542–561. Retrieved from https://doi.org/10.1093/gji/ggw292 doi: 10.1093/gji/ggw292

Hoggard, M. J., Czarnota, K., Richards, F. D., Huston, D. L., Jaques, A. L., & Ghelichkhan, S. (2020, June). Global distribution of sediment-hosted metals controlled by craton edge stability. *Nat. Geosci.*, *13*(7), 504–510. Retrieved from https://doi.org/10.1038/s41561-020-0593-2 doi: 10.1038/s41561-020-0593-2

Jenkins, J., Cottaar, S., White, R., & Deuss, A. (2016). Depressed mantle discontinuities beneath Iceland: Evidence of a garnet controlled 660 km discontinuity? *Earth Planet. Sci. Lett.*, *433*, 159–168. Retrieved from https://doi.org/10.1016/j.epsl.2015.10.053 doi: 10.1016/j.epsl.2015.10.053

Katsura, T., & Ito, E. (1989, November). The system Mg_2SiO_4-Fe_2SiO_4 at high pressures and temperatures: Precise determination of stabilities of olivine, modified spinel, and spinel. *J. Geophys. Res. Solid Earth*, *94*(B11), 15663–15670. Retrieved from https://doi.org/10.1029/jb094ib11p15663 doi: 10.1029/jb094ib11p15663

Matthews, S., Shorttle, O., & Maclennan, J. (2016, November). The temperature of the icelandic mantle from olivine-spinel aluminum exchange thermometry. *Geochem. Geophys. Geosyst.*, *17*(11), 4725–4752. Retrieved from https://doi.org/10.1002/2016gc006497 doi: 10.1002/2016gc006497

Priestley, K., McKenzie, D., & Ho, T. (2018). A lithosphere–asthenosphere boundary—A global model derived from multimode surface-wave tomography and petrology. *Lithospheric discontinuities*, 111–123. Retrieved from https://doi.org/10.1002/9781119249740.ch6 doi: 10.1002/9781119249740.ch6

Schaeffer, A., & Lebedev, S. (2014, September). Imaging the North American continent using waveform inversion of global and USArray data. *Earth Planet. Sci. Lett.*, *402*, 26–41. Retrieved from https://doi.org/10.1016/j.epsl.2014.05.014 doi: 10.1016/j.epsl.2014.05.014

Schaeffer, A. J., & Lebedev, S. (2013, April). Global shear speed structure of the upper mantle and transition zone. *Geophys. J. Int.*, *194*(1), 417–449. Retrieved from https://doi.org/10.1093/gji/ggt095 doi: 10.1093/gji/ggt095

van Stiphout, A. M., Cottaar, S., & Deuss, A. (2019, August). Receiver function mapping of mantle transition zone discontinuities beneath Alaska using scaled 3-D velocity corrections. *Geophys. J. Int.*, *219*(2), 1432–1446. Retrieved from https://doi.org/10.1093/gji/ggz360 doi: 10.1093/gji/ggz360